Danmarks Tekniske Universitet

Master's Thesis

Validation of Wave Simulation Code Based on Experimental Data

Author:

Joaquim Albardaner i Torras

Supervisor:

Dr. Rune Brincker

Civil Engineering DTU

January 2019

Acknowledgements

This is my master's thesis, which will mark the end of a very important stage of my life: my university years, as a student at least. I decided to do it on an exchange because I had heard good reviews of the DTU Civil Engineering Department and I was definitely not disappointed. Nine months ago, when I sent a E-mail to multiple DTU Civil professors asking to do the thesis with them I only received one answer.

That response was from professor Evangelos Katsanos, and thanks to him, I have been able to meet this passionate team of professors and researchers who enjoy their profession. Enthusiastic enough to meet weekly to educate each other with their new findings and debate over different approaches to a problem.

I would like to thank Rune Brincker for organising these meetings where I could gain a grasp of what Operational Modal Analysis was and could feel as a member of this team of researchers. I would like to thank Evangelos for his great encouragement and relaxed way of thinking, making sure that I felt comfortable during all my stay and that I never lacked anything, whilst also keeping a rigid track of my research. I would like to also thank Sandro Amador, who always had time for some of my questions, the answer of which was normally a beer. Obviously the one I am grateful the most is Bruna Nabuco, a hard-working PhD student who guided my thesis and I around the difficult world of cross-correlations and Fast Fourier Transforms. Finally, thanks to Pernille Andersen and Silja Nielses I was able to find the transformation matrix that had me stalled for almost a month. Each one of you has helped me in their own way to make sure I was able to accomplish my task.

Abstract

The objective of this thesis is to validate a wave simulation code. In order to achieve this, the displacements at the top of a monopile were compared between a wave flume model and a finite element model.

Initially, real wave conditions were measured in an offshore wind turbine in the North Sea. This data was applied to create accurate waves in a wave flume at the DTU Mechanical Engineering Laboratory. In the flume, a scaled model of a monopile was positioned and the displacements at the top sampled. After processing the data with MATLAB and applying the Operational Modal Analysis, it was possible to obtain the modal properties of the model, such as mode shapes, natural frequencies and damping ratios.

A finite element model was developed with ANSYS, which accurately recreated the wave flume and was updated to have identical modal properties. The wave simulation code was applied to this finite element model and the displacements at the top were compared with those from the wave flume model.

Index

1. Introduction

The great attention concerning the lifetime of offshore structures, such as oil and gas platforms and wind turbines, has trigged a need for monitoring these structures in order to gain reliable information about their actual state. This would reduce the uncertainty and allow for more optimal decision planning regarding maintenance, repair and future inspection actions.

A methodology based on the robust identification technique of Operational Modal Analysis (OMA) has been previously proposed to predict the strains developed in an offshore structure while an advanced wave simulation code has been developed to generate a high amount of data aiming to verify this proposed methodology.

The purpose of this project was to validate the aforementioned wave simulation code based on experimental data being related to a testing campaign of a scaled model of a monopile structure located in a wave flume. Strains at the base and the top of the monopile, as well as displacements at the head and the elevation of the waves were measured prior to the start of this investigation. A general summary of the process of this thesis can be seen in Figure 1.1.

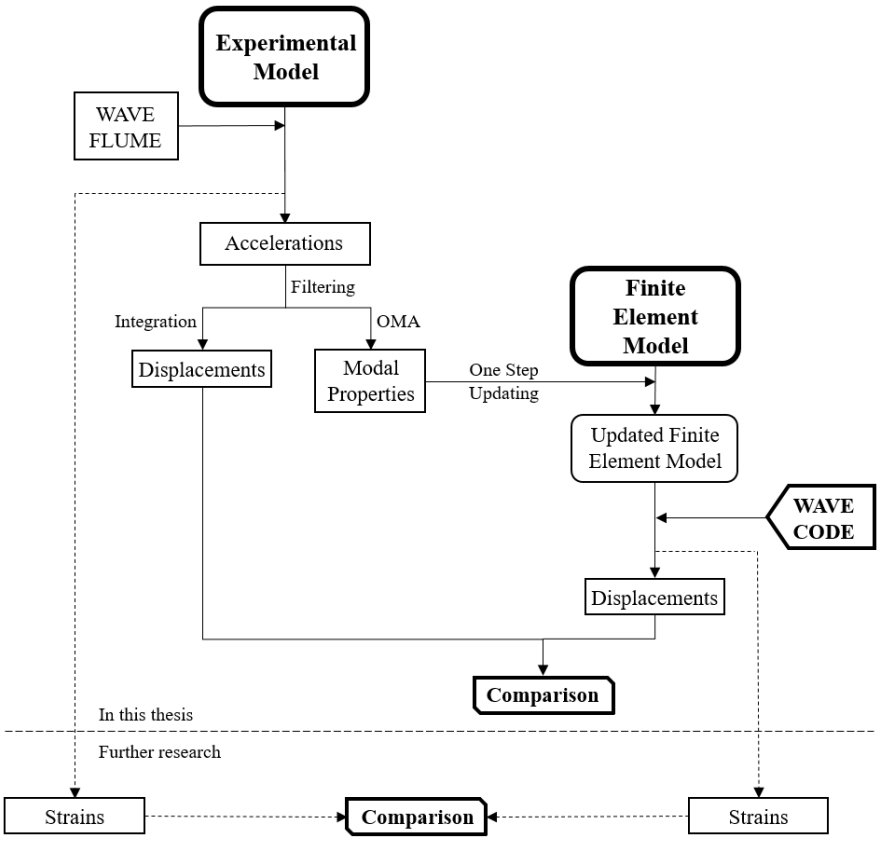

Figure 1.1. General diagram of this project process.

This data was processed in order to apply the OMA, from which the modal properties of the wave flume model were obtained. A Finite Element Model (FEM) was also developed,

which was updated in order to have the same modal properties as the wave flume model. Afterwards, the wave simulation code was applied to the FEM and the resulting displacements were compared with those from the scaled model.

Furthermore, apart from the validation of the wave simulation code, this project aimed to define a correlation between the measurements from the scaled model and the simulations obtained using the finite element model.

Although it is not covered in this thesis, further research could be carried out using the strain data and the already developed finite element model.

2. Experimental Campaign

2.1. Wave Flume Model

The first step of this project was to obtain experimental data in order to see how a scaled monopile behaves inside a wave flume. The generated waves in the scaled model were assumed to be an accurate approximation of a real life scenario. For this, the following model was built (Figures 2.1 and 2.2).

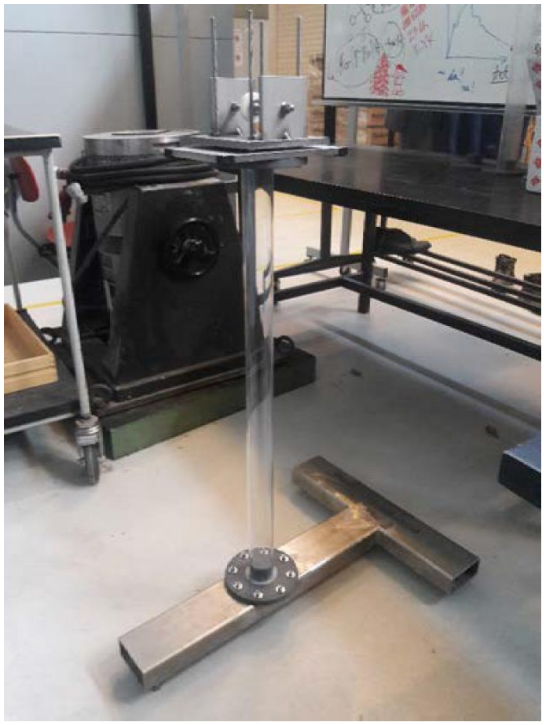

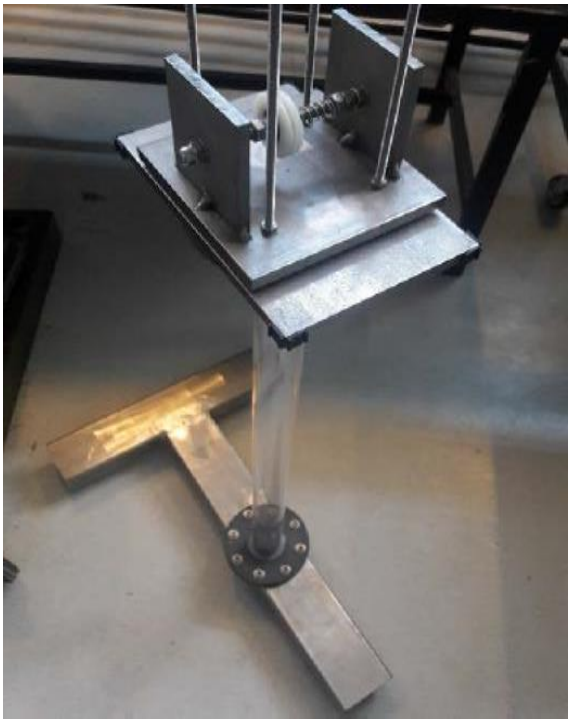

Figures 2.1 & 2.2. Pictures of the model used in the wave flume.

See Appendix A for technical drawings of the model. The characteristics are as follows (Table 2.1):

Scale 1:70	**Real platform**	**Scaled Model**
Water depth (m)	42.0	0.6
Diameter monopile (m)	3.40	0.05
Height (m)	62.55	0.90
Mass on top (kg)	465,000	6.17

Table 2.1. Comparison between characteristics of the real platform and the scaled model used in the wave flume.

The model consisted of a monopile, 80 cm in height; a 2 cm thick steel plate; and two 8 cm vertical plates that held a friction damper, the latter was not used in the scope of this project.

The materials (Table 2.2) were chosen to ensure that the model had a similar natural frequency to the real platform and the mass of the sensors was neglected throughout.

	Monopile	Head
Material	Polycarbonate	Steel
Young's Modulus (MPa)	2,300	210,000
Density (kg/m^3)	1,200	7,850

Table 2.2. Characteristics of the materials used in the wave flume model.

The model was placed in the wave flume at the DTU Mechanical Engineering Laboratory. The flume is 25 m long, 0.6 m wide and 0.8 m high (Figure 2.3).

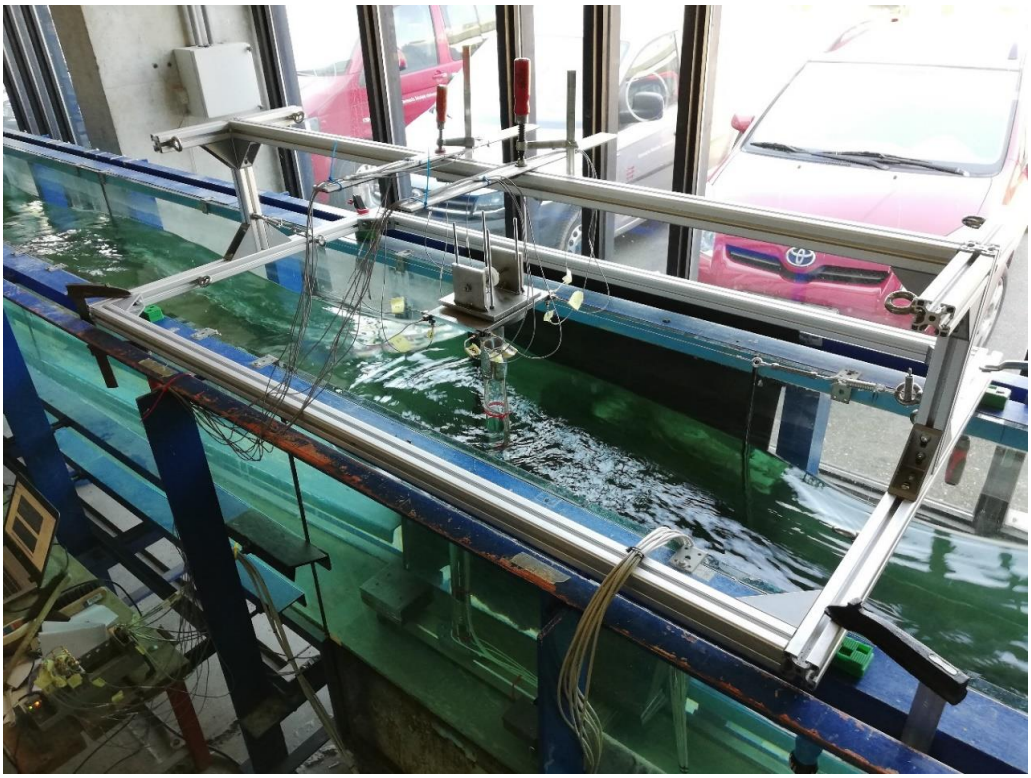

Figure 2.3. Picture of the model inside the wave flume.

To obtain the accelerations at the top of the monopile, the following accelerometers were placed (Figure 2.4).

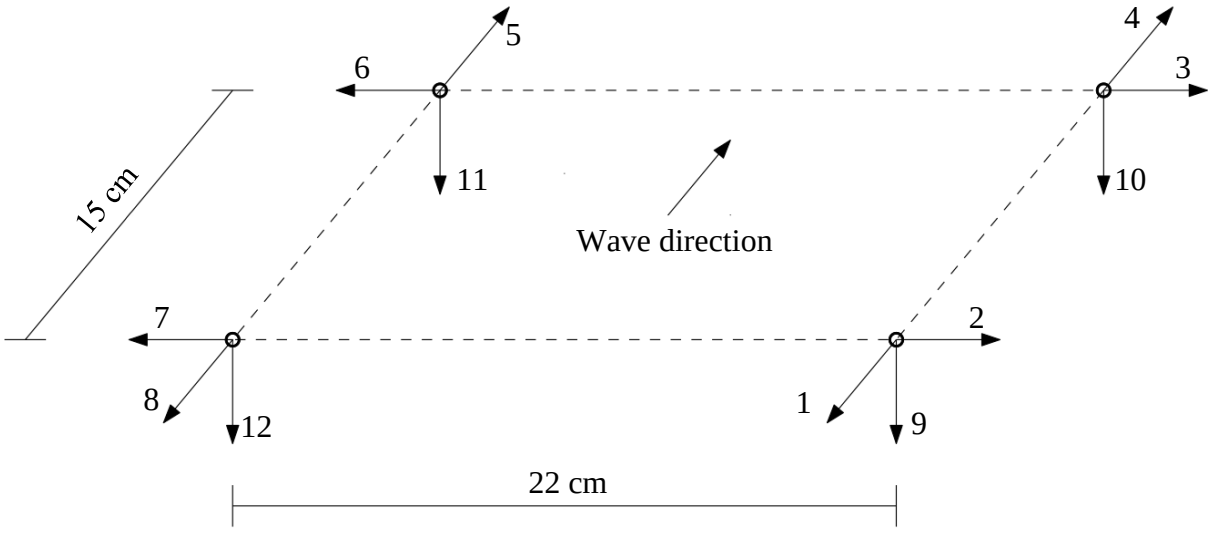

Figure 2.4. Isometric view of the platform with the position of the sensors. Sensors are depicted as black circles.

Furthermore, eight strain gauges were placed in the monopile for the future study of the strains (Figure 2.5), which will not be covered in the content of this thesis.

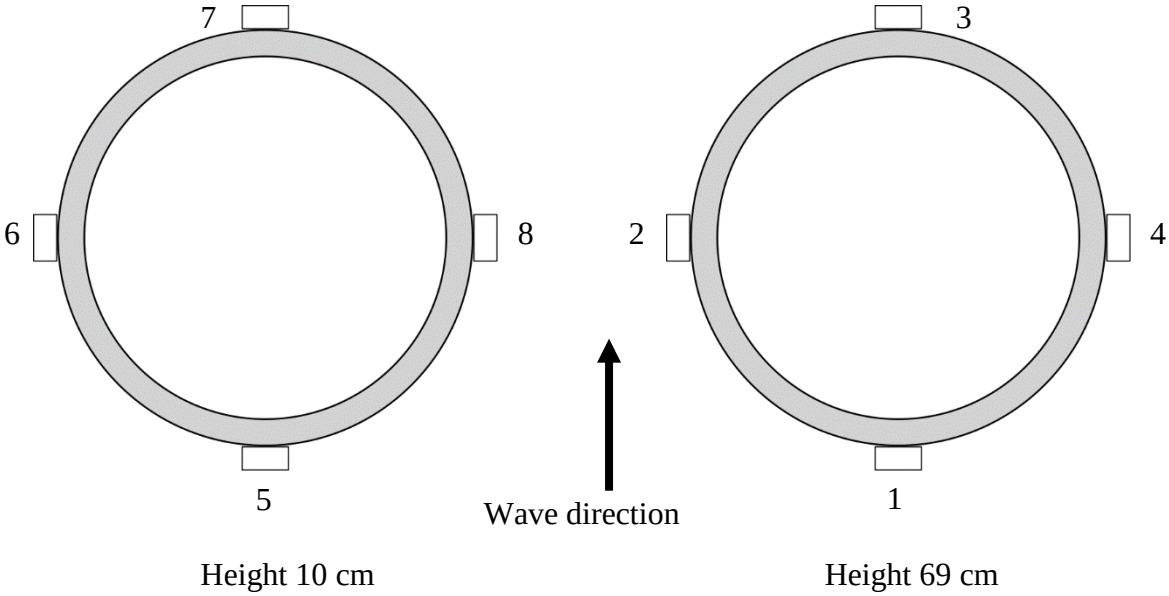

Figure 2.5. Placement of the strain gauges.

2.2. Wave Parameters

For the wave flume and code to be able to simulate the behaviour of the North Sea, known as the JONSWAP spectrum, a wave gauge was placed at the real offshore platform. The gauge took 36 one-hour time series, measuring the wave height and the zero up-crossing period. From this 36 series, the seven cases in Table 3 have been selected [2].

The zero up-crossing period (T_z) is the average time interval between two successive up-crossings of the mean sea level and the peak period (T_p) is determined by the inverse of the frequency with the maximum wave energy. In the JONSWAP spectrum (with $\gamma = 3.3$) the relationship between the zero up-crossing and the peak period can be seen in Equation 2.1 [3]. The significant wave height (H_s) is obtained as the mean of the one-third highest waves (Equation 2.2).

$$T_p = 1.2859 T_z \tag{2.1}$$

$$H_s = \frac{1}{N_{\frac{1}{3}}} \sum_{i=1}^{N_{\frac{1}{3}}} Hi \tag{2.2}$$

Due to the physical limitations of the wave flume, the model was made in a 1:70 scale. This scaling also affected the significant wave height (H_s) and peak period (T_p) before they were introduced to the wave generator.

$$H_{s,model} = \frac{H_{s,real}}{70} \tag{2.3}$$

$$T_{p,model} = \sqrt{\frac{(T_{p,real})^2}{70}} \tag{2.4}$$

	Real Waves		Wave Flume	
Test #	Hs (m)	Tp (s)	Hs (m)	Tp (s)
65 & 71	6.42	10.76	0.092	1.29
66	9.12	13.78	0.130	1.65
67 & 75	5.58	10.52	0.080	1.26
69	4.84	10.17	0.069	1.22
70	1.90	8.37	0.027	1.00
72	5.50	9.80	0.079	1.29
73	2.87	8.37	0.041	1.00

Table 2.3. List of the tests with their properties.

Due to the limitations in the apparatus, it was not possible to create waves with a period inferior to 1 second. Furthermore, this is why tests 70 and 73, whose peak period should be 6 seconds in the real platform, increased to 8.37 seconds.

Once the data was collected, it was treated in order to calculate the displacements of the platform and, using the OMA, the modal properties of the model, such as the natural frequency, the damping ratio and the mode shapes of the structure were also obtained.

2.3. Decimate, Detrend, Filter and Displacements

The first step to process the data was to read it. The accelerometers' readings were stored in a different text file for each test with a column for each sensor. This text file was imported to MATLAB® and introduced in an N by 12 matrix.

The sampling time of the accelerometers was $6.0547 \cdot 10^{-4}$ seconds. This high sampling rate is required to lower the noise floor in future spectral analysis. This sampling rate also creates an elevated number of measurements, too many to work with, so it is necessary to decimate them. Furthermore, this process also improves the use of antialiasing filters as the cut-off frequency can easily be modified knowing the high and fixed sampling rate [1]. In this project, the initial data was decimated by a factor of 80, making the new sampling size 0.0484 seconds.

Another prerequisite needed to apply OMA is to detrend any signal. To detrend means subtracting the mean from a time series. This is done to eliminate the base noise from the sensors and because the frequencies under the lowest of the structure are of no interest. At this point, the data was ready to be studied by OMA.

In a parallel process, as seen in Figure 1.1, after detrending and decimating the data, it was also possible to calculate the displacements. Using a Fast Fourier Transformation (FFT), it was integrated twice in the frequency domain and then, using the inverse, was transformed back to the time domain.

Operating in the frequency domain allowed the peak in the displacements that corresponds to the natural frequency of the model to be seen (Figure 2.6). It could also be observed that the displacements in the x direction are higher than those in the opposing directions.

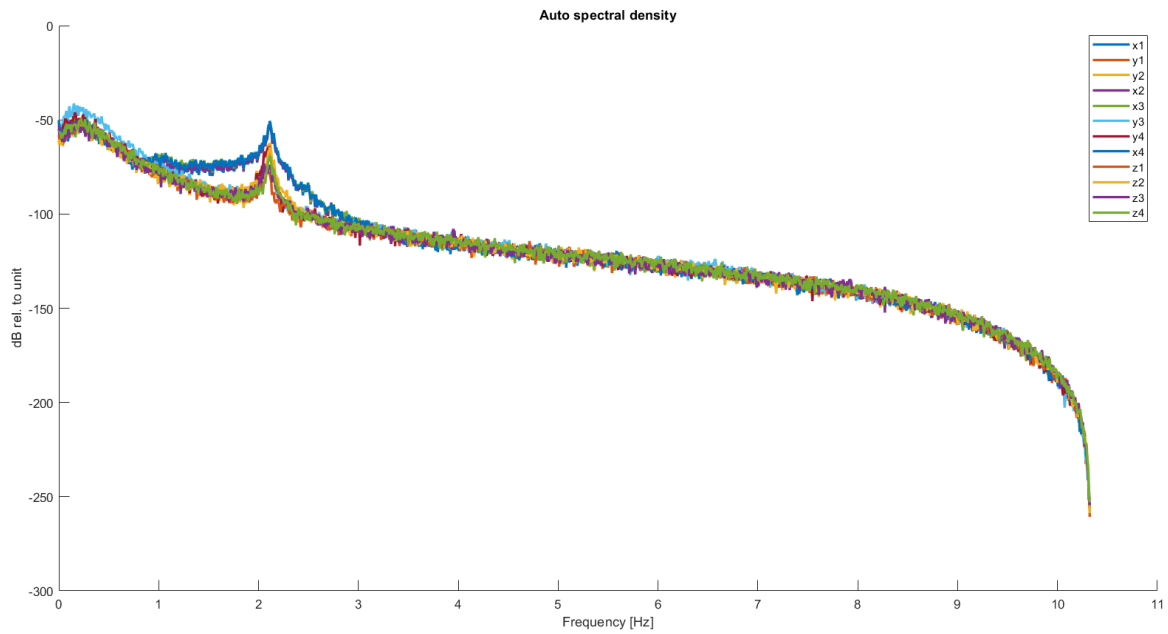

Figure 2.6. Auto spectral density plot of the displacements of every degree of freedom measured. Test 70**.**

In order to disregard any unnecessary data that could slow down or create noise in the process, a band-pass filter was applied. This filter should help diminish the influence of a possible third mode (torsional) that could create rotation in the platform.

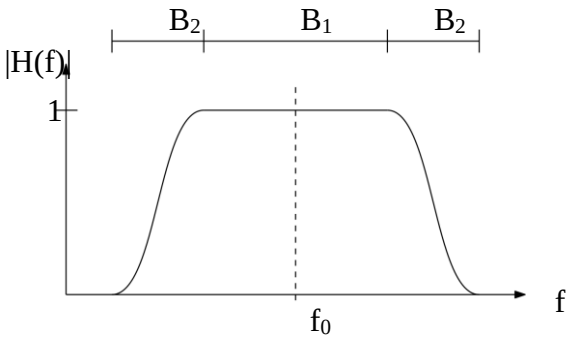

Figure 2.7. Basic schematic that depicts the working of a band-pass filter. *H(f)* corresponds to the frequency respond function of the filter.

In this case, it was needed to eliminate the numerous displacements located at low frequencies due to the noise and the displacements located far away from the point of study (2 Hz). Therefore, the filter was set to pass the signal from 0.7 to 6 Hz. That resulted in f_0 = 3.5 Hz, B_1 = 5.6 Hz and B_2 = 0.1 Hz.

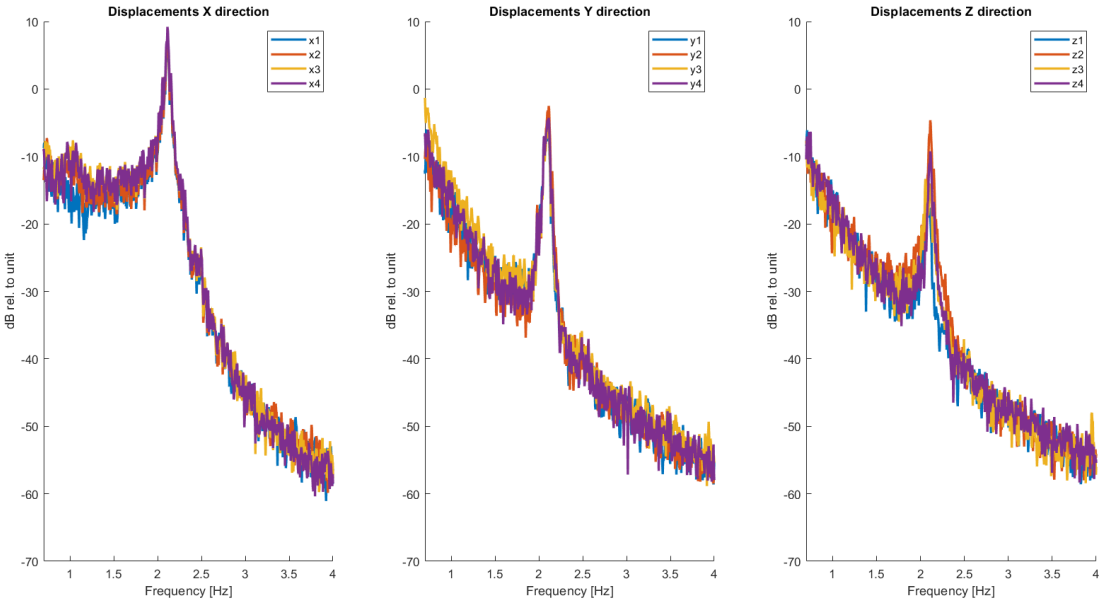

Figure 2.8. Displacements in each direction after applying the band pass filter. Test 70.

Even if 12 Degrees of Freedom (DOF) were measured, only six are needed to determine the position of the platform. Therefore, to avoid over determining the system and to simplify the process, the chosen DOF were x_1, y_1, x_4, z_1, z_2 and z_4. As only three are required to determine the position of a plane, in this project, the two front sensors of the x direction (x_1 and x_4) and the first of the y direction (y_1) were chosen. The three vertical sensors were selected to determine the rotations in the x and y directions.

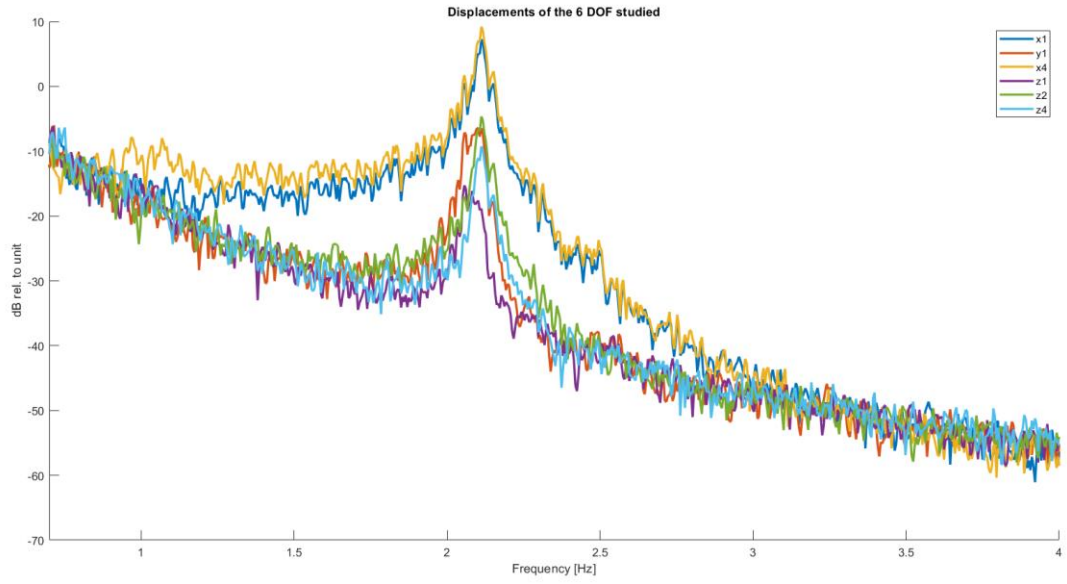

Figure 2.9. Spectral representation of the displacements in the six degrees of freedom chosen. Test 70.

From Figure 2.9, it was possible to assert that at approximately 2 Hz in all directions the displacements experimented an increase in magnitude, especially those in the x. However, in this type of plot, it is difficult to determine that there are two different modes involved hence, the use of a singular matrix plot is appropriate.

Another advantage of having six DOF is that it also simplifies the process to extract singular values from a spectral matrix. Since it calculates the correlation between the different signals, it was possible to observe that there are two different modes with similar frequencies, as can be seen in Figure 2.10. The exact value of these will be found using the OMA, explained in the following chapter.

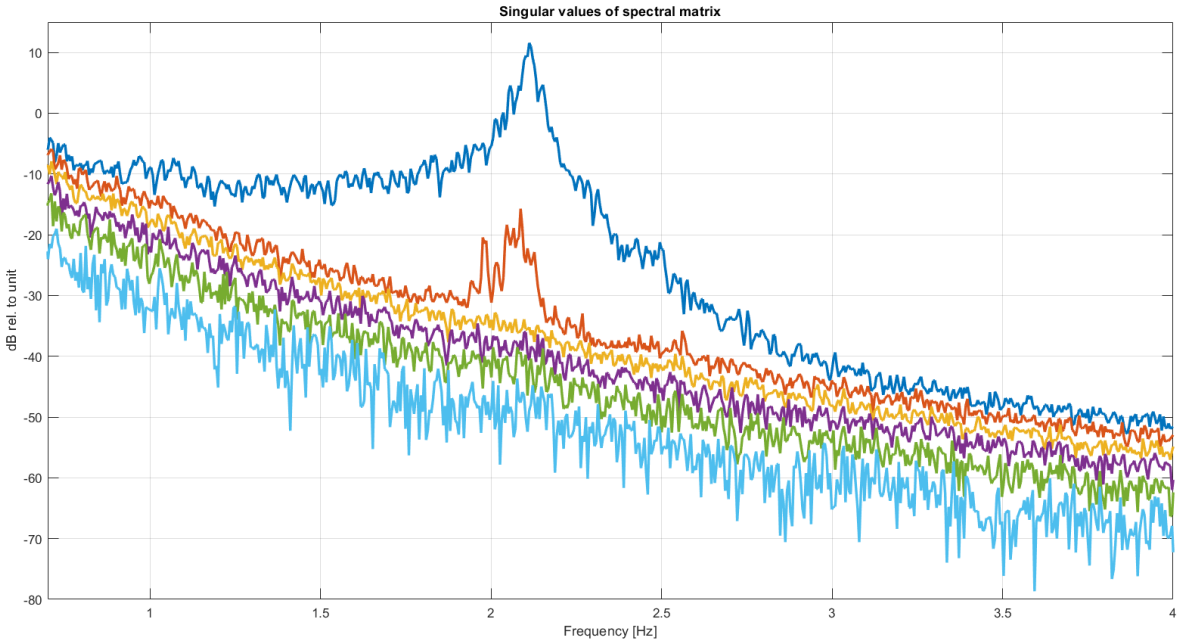

Figure 2.10. Singular values of the spectral matrix of the displacements in the six degrees of freedom chosen. Test 70.

3. Operational Modal Analysis

As stated previously, in order to know the modal properties of the model, the Operational Modal Analysis (OMA) was used [1] [10]. The main advantage of using OMA is that knowing the loads of the system, the stiffness or mass matrix of the structure is not required. All that is necessary to carry out this process, is the response of the system (in this case accelerations) in order to find the mode shapes, natural frequencies and damping ratios of the structure. The only requisite is that the loads need to be random or operate in such a wide range of frequencies that the natural ones are comprehended within the system. It is also relevant to note that within the response of the system both the load and structure properties remain hidden. In the following paragraphs, the theoretical principle of OMA will be explained but will not go into further detail as this deviates from the main objective of this thesis.

To understand OMA it is necessary to appreciate further concepts. Firstly, the correlation function describes the average correlation between two signals when one is delayed τ respect to the other. The response vector being *y(t)*, T the duration of the signal and E the expectation, the correlation matrix can be expressed as:

$$R_y(\tau) = E[y(t)y^T(t+\tau)] = \frac{1}{T}\int_0^T y(t)y^T(t+\tau)dt \tag{3.1}$$

This matrix (N by N) contains the autocorrelation functions in the diagonal and the cross-correlation functions in the off-diagonal. Samples close to each other are more correlated than those far apart. This means that when τ tends to infinity, the correlation tends to zero.

Secondly, the spectral density G(ω) is a Fourier Transform of the correlation function, and can be expressed as:

$$G_y(\omega) = \frac{1}{2\pi}\int_{-\infty}^{\infty} R_y(\tau)e^{i\omega\tau}d\tau \tag{3.2}$$

And also as, with Y(ω) being the Fourier transform of the response:

$$G_y(\omega) = Y^*(\omega)Y(\omega) \tag{3.3}$$

From the spectral density matrix, it is possible to obtain the singular values. This is extremely useful when two nodes are very close together. In Equation 3.4, S is a diagonal matrix with the singular values in the diagonal.

$$S_{yy}(\omega) = U\,S\,U^T \tag{3.4}$$

Once the basic concepts have been covered, the two methods that have been used in this project to find the modal properties of the model: the Time Domain Poly Reference and the Frequency Domain Poly Reference can be explained.

3.1. Time Domain Poly Reference

The Time Domain Poly Reference (TDPR) consists of fitting free decays, represented by correlation functions, with auto regressive models. As Brincker and Ventura approach in their book [1]:

$$y(n) - A_1 y(n-1) - A_2 y(n-2) - \ldots - A_{na} y(n-na) = 0 \tag{3.5}$$

Where y(n) consists of *nc* free decays, n is the time, *na* is the number of previous time instances to considerate, A_k is the auto regressing matrix corresponding to $(n-k)^{th}$.

The next step is to create an overdetermined system where the auto regressing matrices can be estimated.

$$AH_1 = H_2 \tag{3.6}$$

$$\hat{A} = H_2 H_1^* \tag{3.7}$$

Where A is the auto regressing matrix with the shape:

$$A = (A_{na} \quad A_{na-1} \quad \ldots \quad A1) \tag{3.8}$$

H_1 is a Hankel block matrix with *na* block rows:

$$H_1 = \begin{pmatrix} y(1) & y(2) & \ldots & y(np-na) \\ y(2) & y(3) & \ldots & y(np-(na-1)) \\ \vdots & \vdots & \ddots & \vdots \\ y(na) & y(na+1) & \ldots & y(np-1) \end{pmatrix} \tag{3.9}$$

And H_2 is a Hankel block matrix with a single block row:

$$H_2 = (y(na+1) \quad y(na+2) \quad \ldots \quad y(np)) \tag{3.10}$$

Using state space formulation, Equation 3.5 can be rewritten as:

$$A_C u_d(n) = u_d(n+1) \tag{3.11}$$

Where A_C is the companion matrix arranged as:

$$A_C = \begin{pmatrix} 0 & I & 0 & 0 \\ \vdots & 0 & \ddots & \vdots \\ 0 & \vdots & \ddots & I \\ A_{na} & A_{na-1} & \ldots & A_1 \end{pmatrix} \tag{3.12}$$

And $u_d(n)$ is the stacked response vectors:

$$u_d(n) = \begin{Bmatrix} y(n-na+1) \\ \vdots \\ y(n-1) \\ y(n) \end{Bmatrix} = \begin{Bmatrix} be^{(\lambda(-na+1)\Delta t} \\ \vdots \\ y(n-1) \\ y(n) \end{Bmatrix} = e^{\lambda n \Delta t} = \varphi_d \mu^n \tag{3.13}$$

In this last step, it was assumed that free decays can be expressed as $y(n) = be^{\lambda_n \Delta t}$, where λ is the continuous time pole as in $y = e^{\lambda t}$, b is the mode shapes matrix and φ_d is the discrete mode shapes matrix.

Combining equations 3.11 with 3.13, the next equation is obtained:

$$A_c \varphi_d = \mu \varphi_d \tag{3.14}$$

Carrying out an eigenvalue decomposition of the companion matrix, it is possible to obtain the discrete mode shapes as well as the discrete poles from which mode shapes and continuous pole λ can be achieved.

3.2. Frequency Domain Poly Reference

Starting from Equation 2.5, what differentiates this method from the previous one is that the Frequency Domain Poly Reference (FDPR) works in the Z-transform. Here, *e* is the loads of the system and B_k are the moving average matrices.

$$y(n) - \sum_{k=1}^{na} A_k y(n-k) = e(n) + \sum_{k=1}^{nb} B_k e(n-k) \tag{3.15}$$

When transformed to Z space:

$$H\big(f(n)\big) = \left(I - \sum_{k=1}^{na} A_k e^{-ik\omega(n)}\right)^{-1} \left(I + \sum_{k=1}^{nb} B_k e^{-ik\omega(n)}\right) \tag{3.16}$$

Where *f(n)* are the frequencies from zero to the Nyquist frequency and ω(n) are the dimensionless frequencies going from zero to π. The auto regressive (A_k) and moving average (B_k) matrices can be obtained through non-linear optimisation. They can be later assembled into the companion matrix and the modal properties identified just as in the TDPR method.

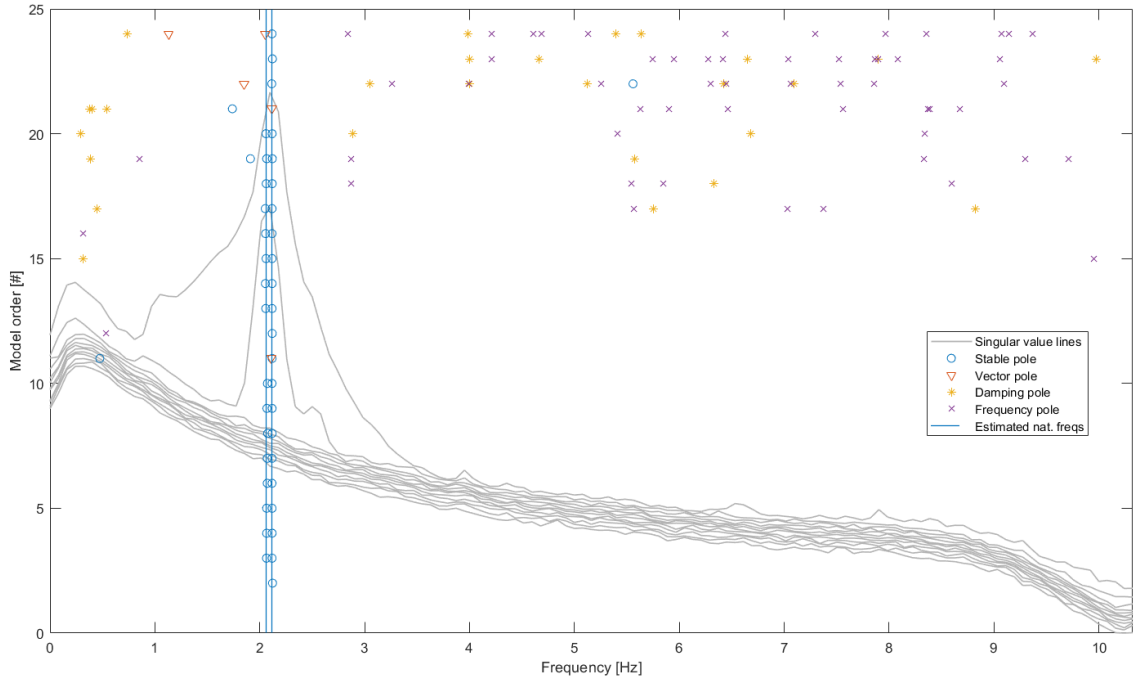

Figure 3.1. Identification of the two main modes using FDPR. Test 70.

TEST	FDPR		TDPR	
	Freq. (Hz)	Damp. (%)	Freq. (Hz)	Damp. (%)
65	2.0622	1.1130	2.0629	1.0588
	2.1098	0.9671	2.1100	0.9923
66	2.0588	1.1030	2.0592	1.0526
	2.1089	0.9132	2.1078	0.8548
67	2.0612	0.9358	2.0626	0.9479
	2.1163	1.0540	2.1153	0.9554
69	2.0656	1.1060	2.0653	0.9685
	2.1143	0.8383	2.1133	0.8694
70	2.0665	0.9428	2.0623	0.8719
	2.1180	0.6196	2.1158	0.7436
71	2.0632	0.8896	2.0659	0.8531
	2.1160	1.0250	2.1128	0.9089
72	2.0632	0.8999	2.0635	0.9768
	2.1083	0.9027	2.1082	0.8826
73	2.0622	0.6741	2.0626	0.7083
	2.1116	0.7962	2.1129	0.7525
75	2.0583	1.0990	2.0581	1.1039
	2.1051	0.8817	2.1049	0.9181
MEAN	2.0624	0.9737	2.0625	0.9491
	2.1120	0.8886	2.1112	0.8753

Table 3.1. List of the natural frequencies and damping ratios identified by the OMA for each test.

3.3. Projection

Even after the band-pass filter was applied, disregarding most of the possible torsion that the monopile could have had, the mode shapes were not precisely projected in the x or y directions, as the ANSYS model will show. This was most likely due to the imperfections of the accelerometers and the direction of the waves, using a wider flume this effect could be reduced. Therefore, a transformation matrix was applied to the mode shapes to force one corner of the platform to stay on the x or y direction, without moving in the other.

The mode shape matrix (12 by 2) being A, T the transformation matrix (2 by 2) and C the directions in which the mode shapes should be projected (12 by 2), it is possible to formulate the following relation:

$$C = AT \tag{3.17}$$

Where:

$$C' = \begin{pmatrix} 1 & 0 & 0 & 0 & 0 & 0 & 0 & 0 & 0 & 0 & 0 & 0 \\ 0 & 1 & 0 & 0 & 0 & 0 & 0 & 0 & 0 & 0 & 0 & 0 \end{pmatrix} \tag{3.18}$$

From this equation it is possible to determine an estimated transformation matrix ($\hat{T}$):

$$\hat{T} = A^* C \tag{3.19}$$

Finally, $\hat{C}$ corresponds to an approximation of the projected mode shapes. These mode shapes are also normalised:

$$\hat{C} = A\hat{T} \tag{3.20}$$

This process is more easily understood graphically.

Mode 1	Mode 2	DOF
0.2573	0.8072	x_1
0.8930	-0.1889	y_1
1.0000	-0.2809	y_2
-0.1595	-0.8725	x_2
-0.1486	-0.9967	x_3
-0.8893	0.2134	y_3
-0.9668	0.2320	y_4
0.1419	1.0000	x_4
0.2591	-0.0030	z_1
0.1505	-0.2069	z_2
-0.2089	-0.0562	z_3
-0.1236	0.1259	z_4

Table 3.2. Mode shapes normalised before the projection. Obtained using TDPR. Test 71.

In Table 3.2, it is noticeable that the first mode corresponds to the displacements in the y direction (ergo rotating around the x direction), while the second mode corresponds to the displacements in the y direction (ergo rotating around the y direction).

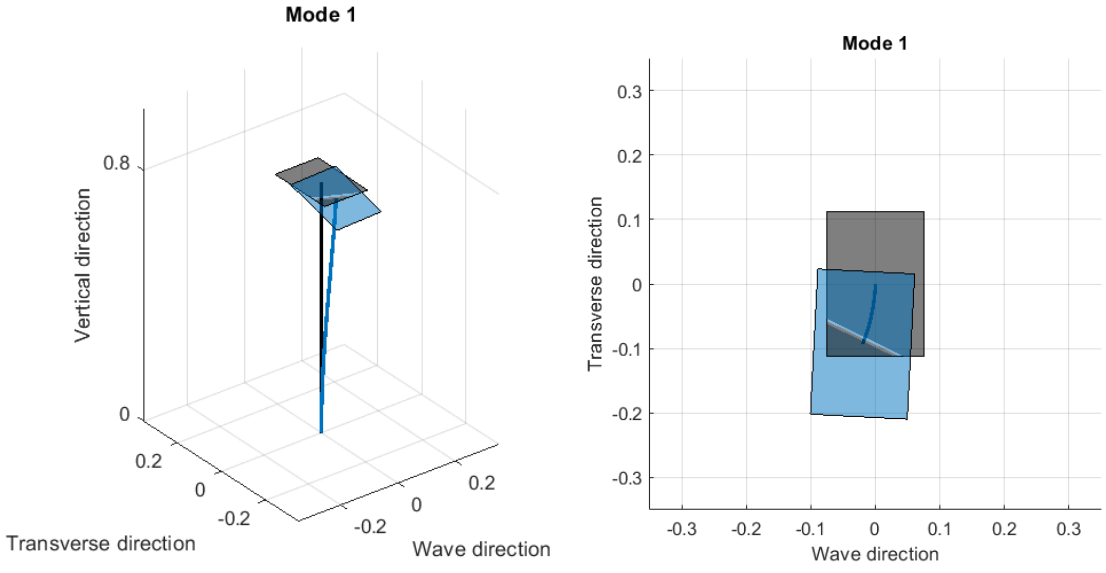

Figure 3.2 & 3.3. Graphic representation of the previously identified first mode shape. Test 71.

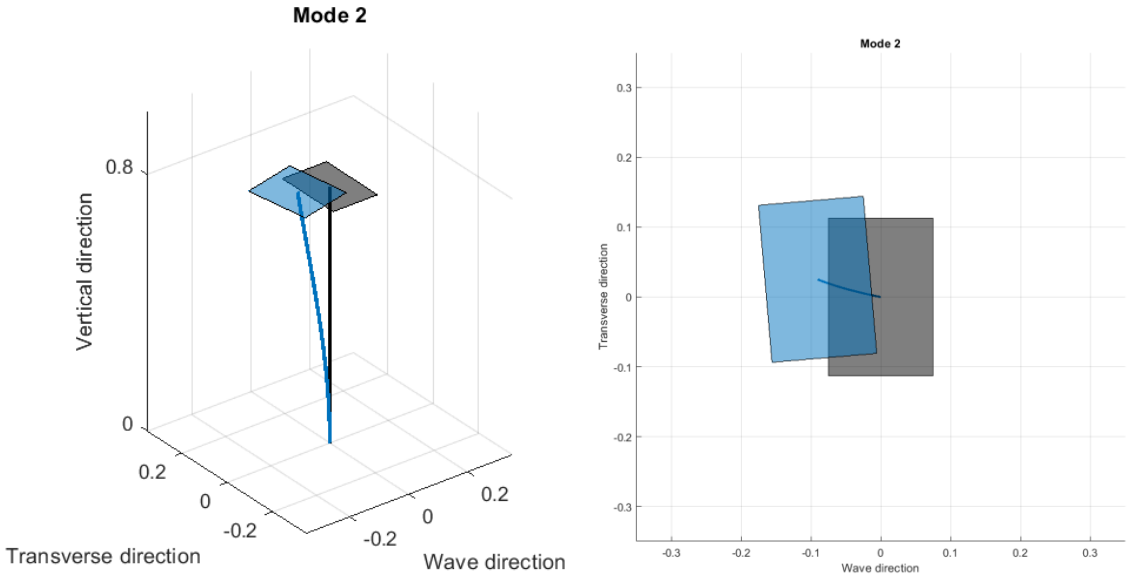

Figure 3.4 & 3.5. Graphic representation of the previously identified second mode shape. Test 71.

In these figures (Figures 3.2 to 3.5) it is seen that, apart from a minimal rotation around the z-axis, there is also translation in both directions x and y at the same time. After applying the aforementioned transformation matrix, the results are as follows.

Mode 1	Mode 2	DOF
0.1310	0.8572	x_1
0.8841	0.1339	y_1
1.0000	0.0839	y_2
-0.0279	-0.8850	x_2
0.0004	-0.9992	x_3
-0.8841	-0.1093	y_3
-0.9611	-0.1187	y_4
-0.0074	1.0000	x_4
0.2491	0.0881	z_1
0.1742	-0.1437	z_2
-0.1924	-0.1267	z_3
-0.1367	0.0763	z_4

Table 3.3. Mode shapes normalised after the projection. Obtained using TDPR. Test 71.

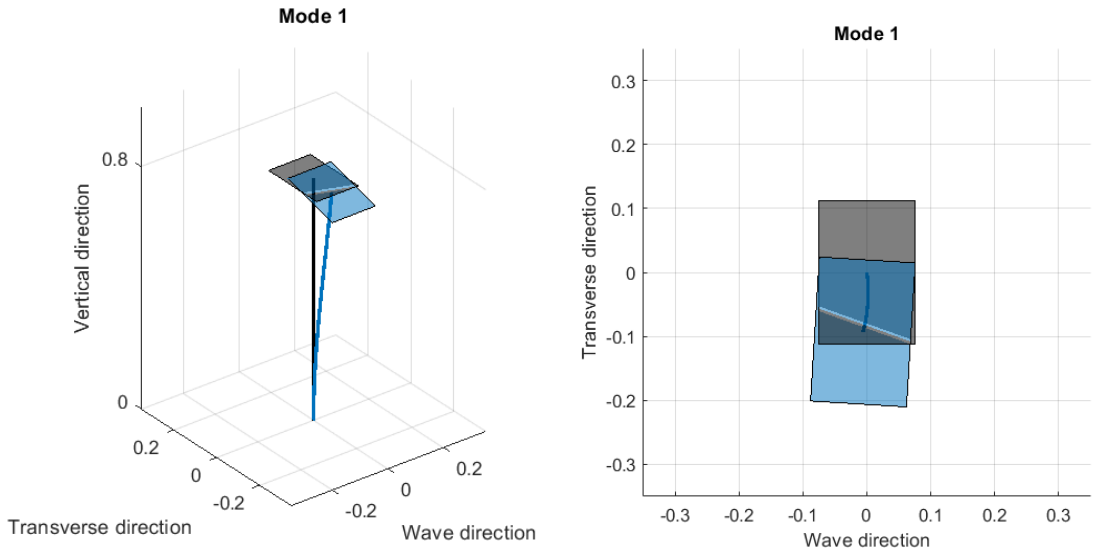

Figure 3.6 & 3.7. Graphic representation of the previously identified first mode shape, after projecting. Test 71.

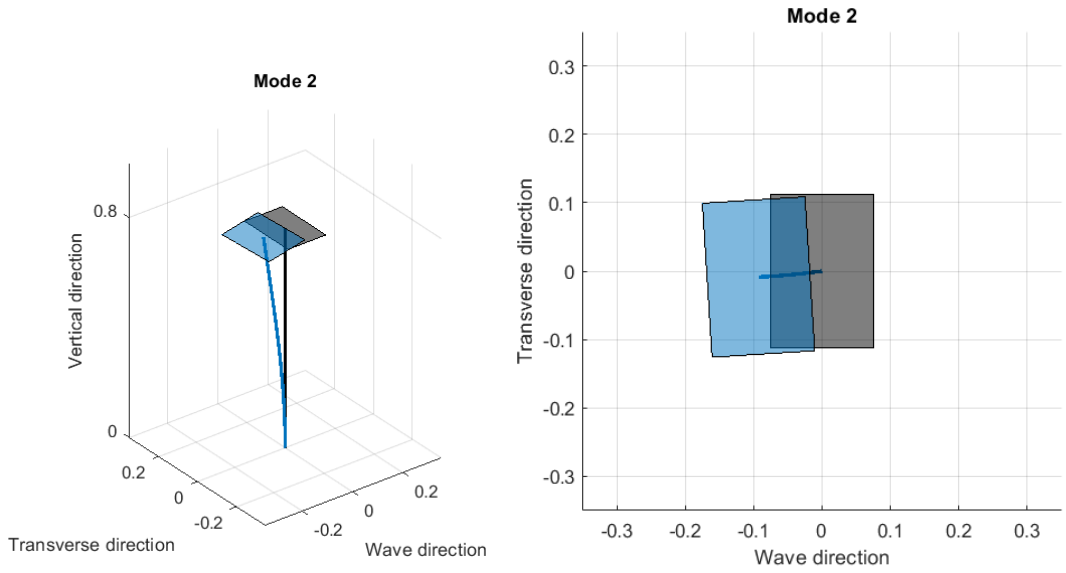

Figure 3.8 & 3.9. Graphic representation of the previously identified second mode shape, after projecting. Test 71.

Once the natural frequencies and mode shapes of the wave flume model have been determined, it is possible to advance to the next step: to create a finite element model true to that of the wave flume.

4. Finite Element Model

In order to apply the developed code, a finite element model was needed. In this project, the software chosen was ANSYS 17.1. This finite element model was made as similar to the flume model as possible and received the forces simulated by the wave script.

Firstly, the elements used to model, were BEAM 188 for the monopile and SHELL 181 for the head plates. Secondly, the materials used were the same as the wave flume model, shown in Table 2.2.

Thirdly, the head of the model was modelled as three plates: one horizontal and two vertical. The vertical plate dimensions consisting of 8.00x8.00x0.80 cm, and the horizontal being 22.00x15.00x2.07 cm. The thickness of the horizontal plate has been defined so the total weight of the head is equal to the one from the flume model (6.17 kg), which is 2.07 cm.

The monopile has the same characteristics as those of the wave flume: outer radius of 2.5 cm and a thickness of 2 mm. The height is 81 cm since the plate has its centre at this location. It is also at that elevation where the two vertical plates emerge from, making the maximum height 90 cm (in agreement with the wave flume model as seen in Table 2.1).

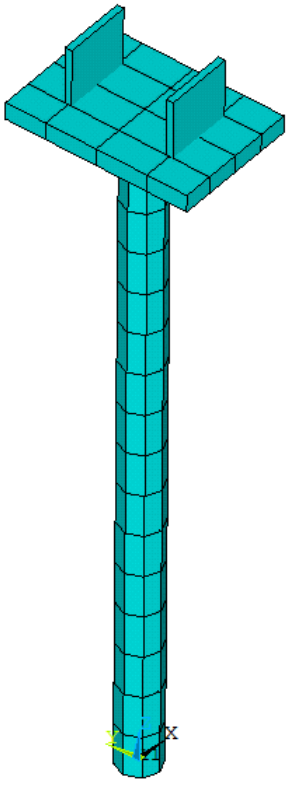

Figure 4.1. Element plot of the developed finite element model.

Once the finite element model was generated, the bottom node was completely clamped and a modal analysis was performed. The mode extraction method used was Block Lanczos, 10 modes have been extracted and their mode shapes expanded. The natural frequencies of these extracted nodes can be seen in Table 4.1.

Mode	Frequency (Hz)
1	2.0979
2	2.1063
3	11.898
4	29.728
5	42.946
6	58.761
7	125.90
8	131.29
9	321.15
10	322.96

Table 4.1. List of the 10 modes extracted from the modal analysis.

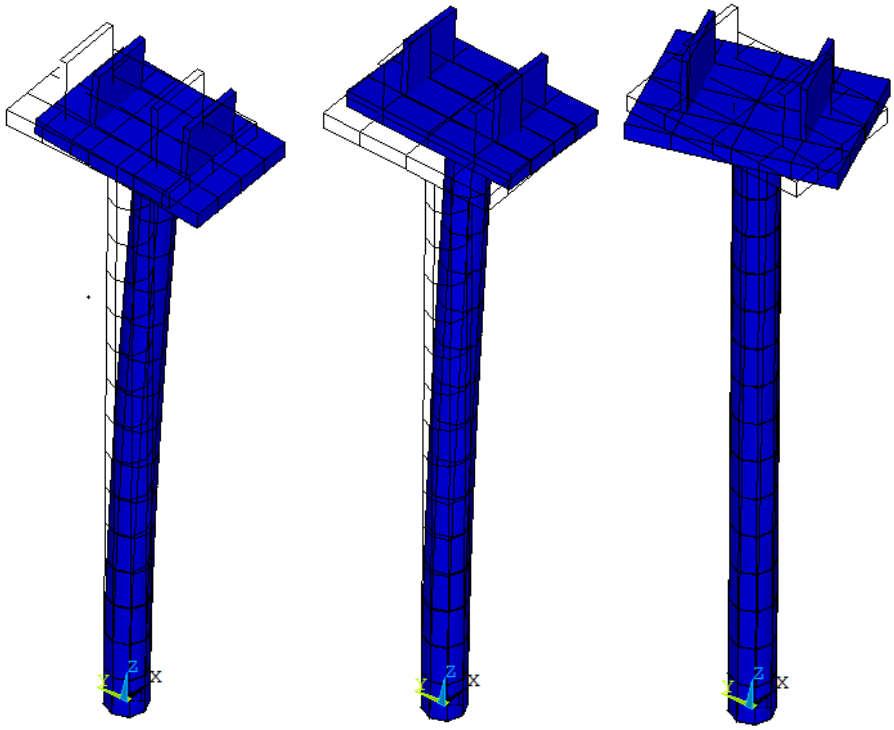

Figure 4.2. Element plot representation of the first three modes extracted.

As can be seen, the first two modes correspond to a bending in the *x* and *y* direction respectively. Logically, since there is more inertia in the *x* direction, the frequency is lower. The third mode, with a wide frequency difference, corresponds to the torsional mode that creates a rotation in the platform.

This finite element model follows the equation of a simple harmonic system:

$$M\ddot{q}(t) - C\dot{q}(t) + Kq(t) = F(t) \tag{4.1}$$

To simplify the model, an undamped system with no friction forces (C=0) and free vibrations (F(t)=0) is considered. Equation 4.1 is reduced to:

$$M\ddot{q}(t) + Kq(t) = 0 \tag{4.2}$$

Which has the following solution:

$$q(t) = Be^{\pm i\omega t} \tag{4.3}$$

Where B is the matrix that has the mode shapes as columns. In this project, these mode shapes will be compared with those from the wave flume.

4.1. Reading the Data from the FEM

From observing Figure 4.2, it can be seen that the first two modes correspond to the first two of the wave flume model (Figures 3.6 & 3.8). Additionally, the corresponding natural frequencies are similar. To proceed with the study, the data was imported to MATLAB.

The imported data consisted of the stiffness matrix (*K*), the mass matrix (*M*) and the mapping matrix. The latter was only used to lower the processing time. Introducing the three nodes that were the subject of study (see Chapter 2.3) and their corresponding degrees of freedom were needed to later compare with the wave flume sensors.

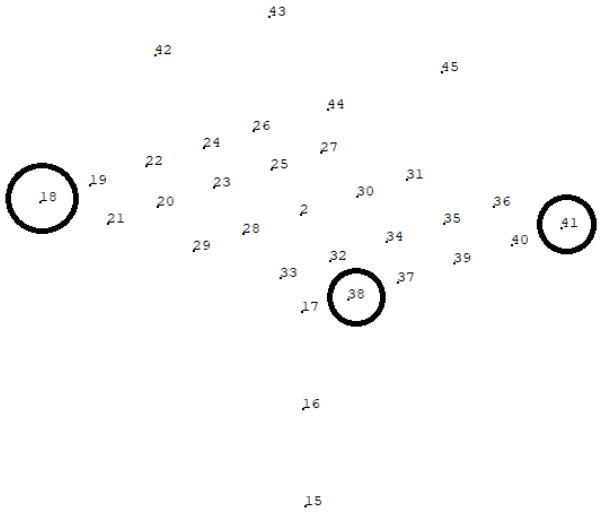

Figure 4.3. Node plot of the platform of the finite element model, with the three nodes subject of study marked with a black circle.

In order to check the similarity between the two mode shape vectors *a* and *b* that should be identical, the Modal Assurance Criterion (MAC) is used. It is possible to calculate the correlation between the two vectors that compose the mode shape as [1]:

$$MAC(a,b) = \frac{|a^H b|^2}{(a^H a)(b^H b)} \tag{4.4}$$

As 12 by 2 matrices were compared, four MAC values resulted. Comparing the first mode shape with the second should give approximately zero, since they are almost perpendicular. This can be clearly seen in Figure 4.4.

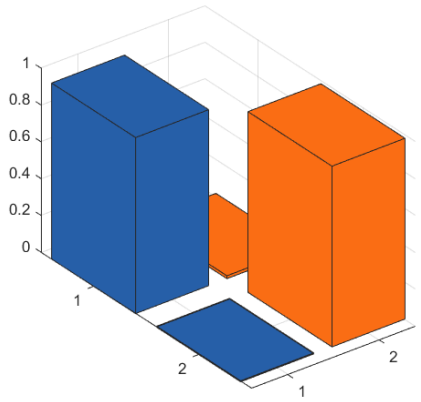

Figure 4.4. Representation of the MAC values comparing the two first mode shapes of the experimental model with the two first mode shapes of the FEM. Test 70.

In Table 4.2, there is a list to examine the MAC values for each test. From these numbers it was possible to observe that the mode shapes of the experimental model and the finite element model were almost identical. Nevertheless, it was possible to achieve a greater match.

4.2. One Step Updating

Once the data from the finite element model had been introduced in the program, it had to be corrected so it contained exactly the same natural frequencies (ω_{ai}) and mode shapes (a_i) as the model used in the wave flume. In this case, only the first two modes were replaced ($i = 1{,}2$).

To access the desired mode shapes and change them to the ones from the experimental model, the following process was used. [4]

Orthogonal equations:

$$B^T M B = I \tag{4.5}$$

$$B^T K B = \begin{bmatrix} \ddots & & \\ & {\omega_i}^2 & \\ & & \ddots \end{bmatrix} \tag{4.6}$$

Where the diagonal modal mass matrix (M) and the diagonal modal stiffness matrix (K) can be isolated and expressed as:

$$M^{-1} = BB^T = \sum_{r=1}^{N} b_r {b_r}^T = \sum_{r=1}^{N_a} b_r {b_r}^T + \sum_{r=N_a+1}^{N} b_r {b_r}^T \tag{4.7}$$

$$K^{-1} = B \begin{bmatrix} \ddots & & \\ & {\omega_i}^2 & \\ & & \ddots \end{bmatrix} B^T = \sum_{r=1}^{N} b_r {b_r}^T \omega^{-2} = \sum_{r=1}^{N_a} b_r {b_r}^T \omega^{-2} + \sum_{r=N_a+1}^{N} b_r {b_r}^T \omega^{-2} \tag{4.8}$$

Where N_a is the number of modes to change (in this case N_a=2) and b_r are each of the finite element modes from one to N. Before replacing the two desired modes, it was needed to expand the ones from the experiments.

4.2.1. Expansion

The expansion was required because the modes from the experimental model were rank 12 (as this was the number of accelerometers) but those from the finite element had as many degrees of freedom as were in the FEM. In this case, the FEM had 45 nodes with six DOF per node. Deducting the six DOF at the bottom node because it was fully clamped equalled 264.

In order to perform the expansion, a transformation matrix T was deduced to increase the rank of the experimental mode shapes from 12 to 264. With a_{rn} being the mode shapes from the experiments (12 by 1), n being in this case each mode shape (1 and 2), and B_{rn} the reduced modal vector matrix, it was possible to formulate the following equation.

$$a_{rn} = B_{rn} \cdot T \tag{4.9}$$

The reduced modal vector matrix is a cluster of modes ranked 12 by the number of reference modes picked. The most simple cluster would be three, being one mode the equivalent of the mode shape that is to be expanded, and the other two its contiguous. This could also be applied with 2n+1 modes, with the wanted mode shape always in the centre. The rows picked from the FEM modes corresponded to the only DOF measured in the experiments.

$$\hat{T} \approx B_{rn}^{*} \cdot a_{nr} \tag{4.10}$$

Supposing B_{rn} is a 12 by 3 matrix, T results in being a 3 by 1 that can be multiplied by the full mode shapes of the FEM (B_{xn}), giving the mode shapes of the experimental model a 264 rank (a_{xn}).

$$a_{xn} \approx B_{xn} \cdot \hat{T} \tag{4.11}$$

Once the dimensions of the mode shapes matched, it was possible to proceed with the One Step Updating. The process consisted in deleting the non-desired modes from the finite element model and replacing them with the expanded ones from the experimental data [5].

$$M_u{}^{-1} = M^{-1} - \sum_{r=1}^{N_a} b_r b_r{}^{T} + \sum_{r=1}^{N_a} a_{xr} a_{xr}{}^{T} \tag{4.12}$$

$$K_u{}^{-1} = K^{-1} - \sum_{r=1}^{N_a} b_r b_r{}^{T} \omega_r{}^{-2} + \sum_{r=1}^{N_a} a_{xr} a_{xr}{}^{T} \omega_{ar}{}^{-2} \tag{4.13}$$

Once the mass matrix (M_u) and the stiffness matrix (K_u) were updated, a MAC value check was made to ensure that it had increased. It is important to remember that the expansion process is not perfect and the expanded mode shapes are an approximation.

Test	Mode	MAC before updating	MAC after updating
65	1st Mode	0.9732	0.9952
	2nd Mode	0.9812	0.9967
66	1st Mode	0.9759	0.9956
	2nd Mode	0.9825	0.9969
67	1st Mode	0.9737	0.9949
	2nd Mode	0.9814	0.9968
69	1st Mode	0.9741	0.9953
	2nd Mode	0.9815	0.9968
70	1st Mode	0.9697	0.9950
	2nd Mode	0.9790	0.9964
71	1st Mode	0.9741	0.9953
	2nd Mode	0.9817	0.9969
72	1st Mode	0.9753	0.9953
	2nd Mode	0.9825	0.9969
73	1st Mode	0.9740	0.9955
	2nd Mode	0.9815	0.9968
75	1st Mode	0.9755	0.9954
	2nd Mode	0.9823	0.9968

Table 4.2. Comparison between the MAC value before and after the One-Step Updating.

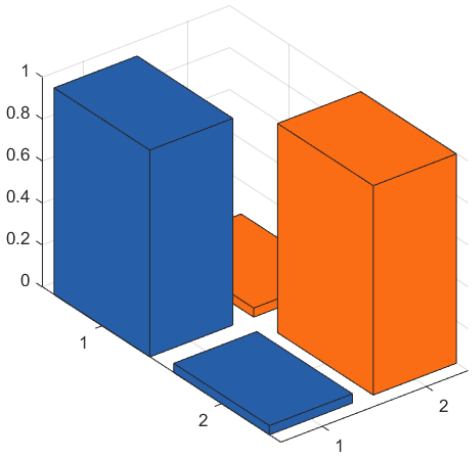

Figure 4.5. Representation of the MAC values comparing the two first mode shapes of the experimental model with the two first mode shapes of the FEM after being updated. Test 70.

Since the MAC value increased and became almost unity, it was possible to state that the finite element model had the same mode shapes as the wave flume model, and it was suitable to perform under the wave simulation code.

5. Wave Simulation Code

As it has been stated previously, the ultimate objective of this thesis is the validation of a wave simulation code. This script is fundamental in simulating the forces that the sea applies to an offshore structure. Furthermore, the aforementioned code was essential to test the capabilities of the robust identification technique OMA.

This wave simulation code defines the sea state from a wave spectrum. Afterwards, using the basic wave kinematics formulae, the parameters to apply the Morison forces were obtained. These forces were combined with the mode shapes; natural frequencies and damping ratios of the finite element model to be finally integrated using the FFT to provide the displacements in each node of the finite element model monopile.

Waves are created by the wind, so their behaviour differs depending on the ocean or sea of study. This wave simulation code is focused on the North Sea, which can be parameterised by a spectrum known as the Joint North Sea Wave Project (JONSWAP).

This spectrum is the distribution of power into frequencies of the signal. The most widely used was proposed by Pierson and Moskowitz on 1964 [6]. Nine years later, Hasselmann during the JONSWAP [7], found out that the sea was never fully developed, meaning that the waves never reach an equilibrium with the wind and thus staying in a transient state. The JONSWAP spectrum is essentially a Pierson-Moskowitz spectrum with a correction factor (γ^r) and a normalising factor (A_γ) [3].

Being $S(\omega)$ the energy of the waves with respect to frequency, U_{10} the speed of the wind 10 metres above the sea level, g the gravity and F the distance from a lee shore (distance over which the wind blows with constant speed) [7][8]:

$$S(\omega) = A_\gamma \cdot \frac{\alpha g^2}{\omega^5} e^{-\frac{5}{4}\left(\frac{\omega_p}{\omega}\right)^4} \cdot \gamma^r \tag{5.1}$$

Where,

$$r = e^{-\frac{(\omega-\omega_p)^2}{2\sigma^2\omega_p^2}}; \quad A_\gamma = 1 - 0.287\ln(\gamma) \tag{5.2}$$

and

$$\alpha = 0.076\left(\frac{U_{10}^2}{Fg}\right)^{0.22}; \quad \omega_p = 22\left(\frac{g^2}{U_{10}F}\right)^{1/3}; \quad \gamma = 3.3 \tag{5.3}$$

$$\sigma = \begin{cases} 0.07 & \omega \leq \omega_p \\ 0.09 & \omega > \omega_p \end{cases}$$

The following relations are known:

$$\alpha\, g^2 = \frac{5}{16} H_s^2 \omega_p^4; \quad \omega_p = \frac{2\pi}{T_p} \tag{5.4}$$

Thus, combining equation 5.1 with relations 5.3, it is not needed to know U_{10} or F, only the significant wave height (H_s) and the mean peak period (T_p). See Equation 1 on how to obtain T_p.

$$S(\omega) = A_\gamma \cdot \frac{5}{16} \frac{H_S^2 \omega_p^4}{\omega^5} e^{-\frac{5}{4}\left(\frac{\omega p}{\omega}\right)^4} \cdot \gamma^r \tag{5.5}$$

Other needed parameters in order to calculate the forces that the waves will apply to the structure are the horizontal particle velocity and acceleration, calculated with the following formulae, taken from [3].

$$u(t,z,x) = \sum_{i=1}^{N/2} \sqrt{2S_i d\omega} \cdot \cos(\omega_i t - k_i x - \varphi_i) \cdot \omega \cdot \frac{\cosh\big(k(z+d)\big)}{\sinh(k \cdot d)} \tag{5.7}$$

$$dudt(t,z,x) = -\sum_{i=1}^{N/2} \sqrt{2S_i d\omega} \cdot \sin(\omega_i t - k_i x - \varphi_i) \cdot \omega^2 \cdot \frac{\cosh\big(k(z+d)\big)}{\sinh(k \cdot d)} \tag{5.8}$$

Where *u* is the fluid's horizontal particle velocity (m/s), *dudt* the fluid's horizontal particle acceleration (m/s^2), *z* the vertical coordinate positive upward (with origin at still water level, will vary for each node in the monopile), *S(ω)* the wave spectrum, *ω* the angular frequency, *k* the wavenumber, *x* the longitudinal position, *d* the water depth and *φ* the wave phase.

Finally, it is possible to apply Morison's Equations. f_d being the drag force and f_i the inertia force:

$$f_d(t) = \frac{1}{2}\, \rho\, C_D\, D\, u\, |u| \tag{5.8}$$

$$f_i(t) = \rho\, (1 + C_A)\, A\, dudt \tag{5.9}$$

Where ρ is the fluid's density (kg/m^3), C_A is the added mass coefficient (2.00), C_D is the drag coefficient of a cylinder (1.00) [3], D is the outer diameter of the monopile (0.05 m) and A is the cross section area (0.002 m^2). The overall force exerted on each node of the monopile will be the addition of the two previous forces.

$$f_N(t) = f_d(t) + f_i(t) \tag{5.10}$$

Combining the mode shape matrix (B_s) and the natural frequencies with the aforementioned forces, it is possible to calculate the displacements of each node using the FFT.

6. Comparative Assessment

The final step to be able to validate the wave simulation code is to compare the displacements of the scaled model produced by the wave flume and the displacements calculated in the finite element model after applying the wave simulation code.

6.1. Calculating the Displacements in the Centre of the Plate

In Chapter 2, the data was filtered to remove the displacements that resulted from the 3rd mode (the torsional one). Nevertheless, it is impossible to completely eliminate it and some noise remains. Since the simulated displacements do not have this error, it is more accurate to compare the displacements in the centre of the top plate. This way any rotation around the z-axis is reduced or nullified. Therefore, before it was possible to compare the displacements between the models, it was necessary to find the displacements in the centre of the plate of the wave flume model.

The following transformation matrix (T) was deduced to find the displacements in the centre (θ) from the displacements in the sensors (y).

$$y = T \cdot \theta \tag{6.1}$$

$$y' = \{x_1\ y_1\ y_2\ x_2\ x_3\ y_3\ y_4\ x_4\ z_1\ z_2\ z_3\ z_4\}; \qquad \theta' = \{x\ y\ z\ \theta_x\ \theta_y\ \theta_z\} \tag{6.2}$$

The displacements in the corners matrix (y) is sorted by sensor number, as seen in Figure 6.1. Its dimension is 12 by the number of samples taken. The size of the displacements in the centre matrix (θ) is 6 by the number of samples. Therefore, the transformation matrix T will be a 12 by 6. To calculate the aforementioned matrix first it is crucial to know the direction of the sensors. The global coordinate system will be the same as the finite element model one, which can be seen in Figure 4.1.

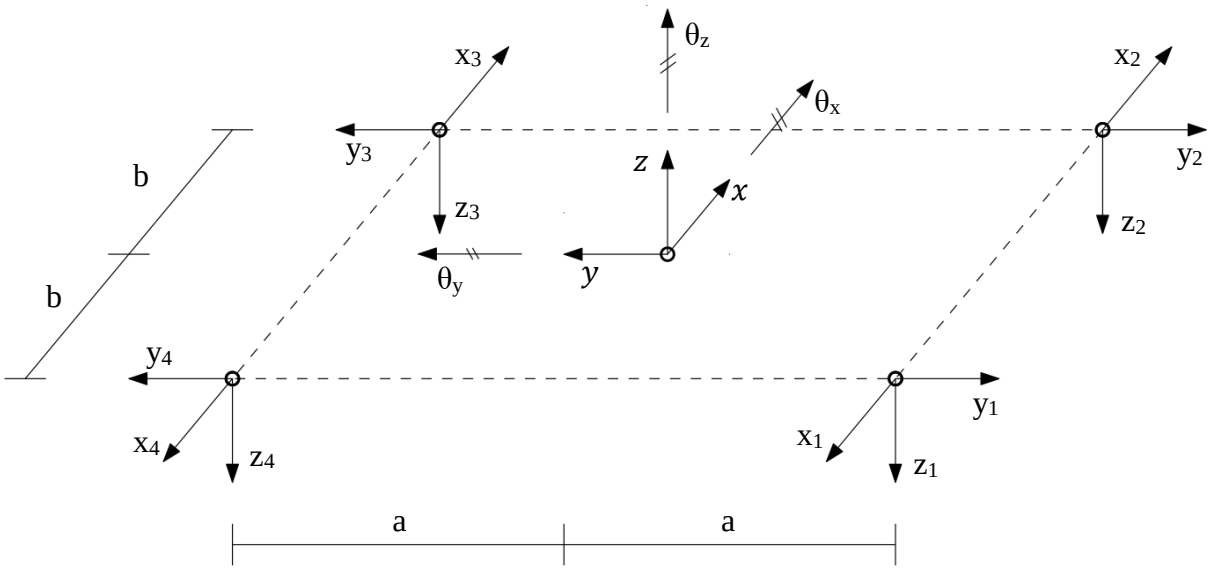

Figure 6.1. Distribution of the 12 sensors on the platform.

Since the plate is made of steel, it was considered as a completely rigid solid. This meant that if a displacement was applied in any of the directions, it would be the same in the entire solid, regardless of what point was to be studied.

To know the relation to the rotation of the centre and the displacements in the corners the rotation matrix for a plane will be applied. Knowing that the displacements are small compared to the size of the plate, it is correct to use the approximation of infinitesimal rotations. Since θ≈0:

$$A = \begin{pmatrix} cos\theta & -sin\theta \\ sin\theta & cos\theta \end{pmatrix} \approx \begin{pmatrix} 1 & -\theta \\ \theta & 1 \end{pmatrix} \tag{6.2}$$

$$f_i = \hat{v}_i - v_i = Av_i - v_i \tag{6.3}$$

6.1.1. Rotation around the *x* axis

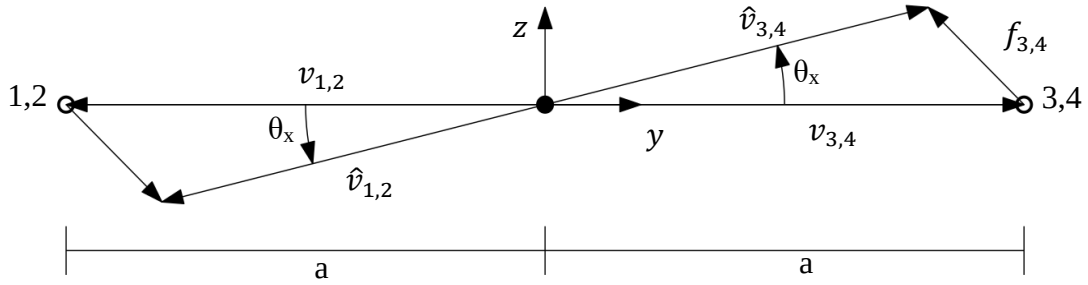

Figure 6.2. Rotation around de *x*-axis. Corners depicted as black circles.

$$v_{1,2} = \begin{pmatrix} -a \\ 0 \end{pmatrix}, \qquad v_{3,4} = \begin{pmatrix} a \\ 0 \end{pmatrix}$$

$$f_{1,2} = \begin{pmatrix} y_{1,2} \\ z_{1,2} \end{pmatrix} = \begin{pmatrix} 0 \\ -a\theta_x \end{pmatrix}, \qquad f_{3,4} = \begin{pmatrix} y_{3,4} \\ z_{3,4} \end{pmatrix} = \begin{pmatrix} 0 \\ a\theta_x \end{pmatrix}$$

6.1.2. Rotation around the *y* axis

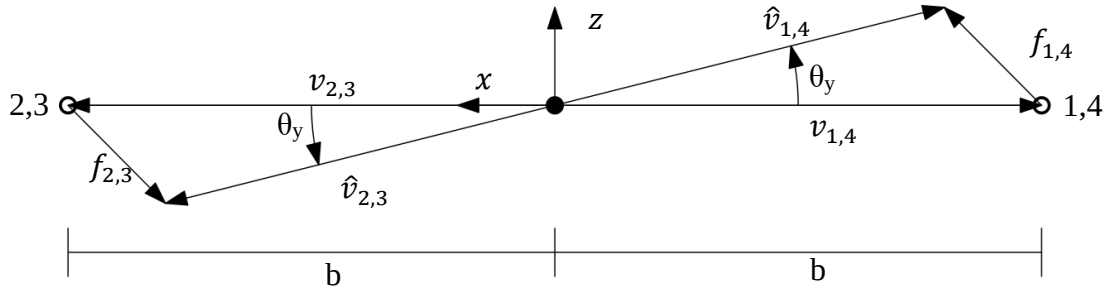

Figure 6.3. Rotation around de *y*-axis. Corners depicted as black circles.

$$v_{1,4} = \begin{pmatrix} 0 \\ -b \end{pmatrix}, \qquad v_{2,3} = \begin{pmatrix} 0 \\ b \end{pmatrix}$$

$$f_{1,4} = \begin{pmatrix} z_{1,4} \\ y_{1,4} \end{pmatrix} = \begin{pmatrix} b\theta_y \\ 0 \end{pmatrix}, \qquad f_{2,3} = \begin{pmatrix} z_{2,3} \\ y_{2,3} \end{pmatrix} = \begin{pmatrix} -b\theta_y \\ 0 \end{pmatrix}$$

6.1.3. Rotation around the *z* axis

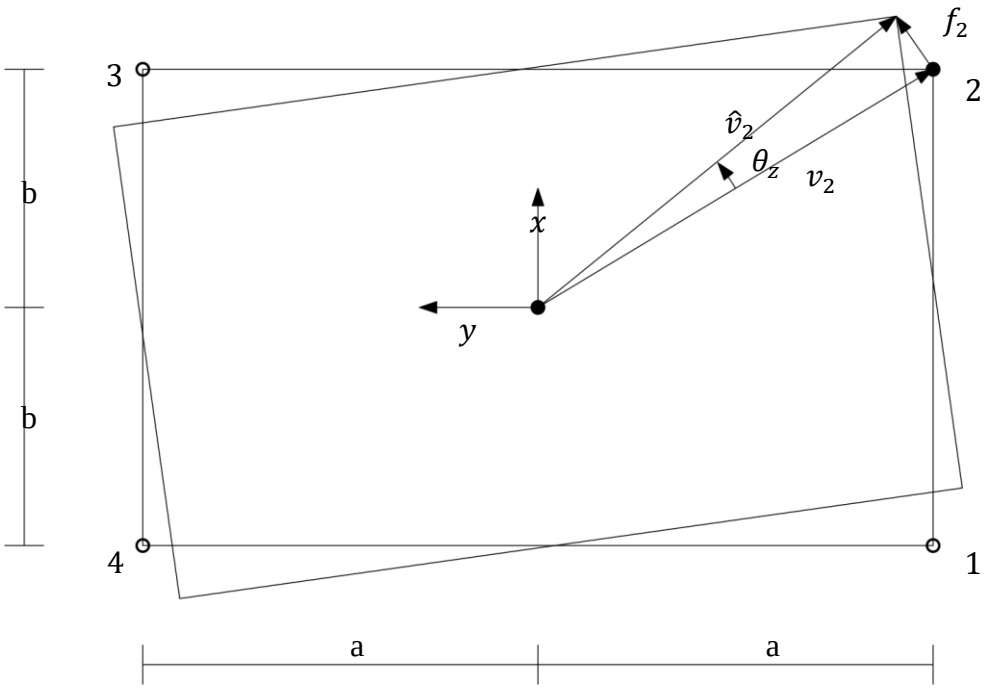

Figure 6.4. Rotation around de *z*-axis. Corners depicted as black circles.

$$v_1 = \begin{pmatrix} -b \\ -a \end{pmatrix}, \qquad v_1 = \begin{pmatrix} b \\ -a \end{pmatrix}, \qquad v_1 = \begin{pmatrix} b \\ a \end{pmatrix}, \qquad v_1 = \begin{pmatrix} -b \\ a \end{pmatrix}$$

$$f_1 = \begin{pmatrix} x_1 \\ y_1 \end{pmatrix} = \begin{pmatrix} a\theta_z \\ -b\theta_z \end{pmatrix}, \qquad f_2 = \begin{pmatrix} x_2 \\ y_2 \end{pmatrix} = \begin{pmatrix} a\theta_z \\ b\theta_z \end{pmatrix}$$

$$f_3 = \begin{pmatrix} x_3 \\ y_3 \end{pmatrix} = \begin{pmatrix} -a\theta_z \\ b\theta_z \end{pmatrix}, \qquad f_4 = \begin{pmatrix} x_4 \\ y_4 \end{pmatrix} = \begin{pmatrix} -a\theta_z \\ -b\theta_z \end{pmatrix}$$

Combining the previous vectors, the following transformation matrix results:

$$T = \begin{pmatrix} -1 & 0 & 0 & 0 & 0 & a \\ 0 & -1 & 0 & 0 & 0 & -b \\ 0 & -1 & 0 & 0 & 0 & b \\ 1 & 0 & 0 & 0 & 0 & a \\ 1 & 0 & 0 & 0 & 0 & -a \\ 0 & 1 & 0 & 0 & 0 & b \\ 0 & 1 & 0 & 0 & 0 & -b \\ -1 & 0 & 0 & 0 & 0 & -a \\ 0 & 0 & -1 & -a & b & 0 \\ 0 & 0 & -1 & -a & -b & 0 \\ 0 & 0 & -1 & a & -b & 0 \\ 0 & 0 & -1 & a & b & 0 \end{pmatrix} \tag{6.4}$$

In the experiments performed, as well as the finite element model, *a* was equal to 0.11 meters and *b* was equal to 0.075 meters. Furthermore, another matrix was calculated using only the 6 degrees of freedom subject of study (x_1, y_1, x_4, z_1, z_2, z_4), called “reduced” (6 by 6).

6.1.4. Validation of the Transformation Matrix

To check if the previously found transformation matrix was correct, another method to calculate the displacements in the centre of the platform was used. The method consists in expanding the displacements of the experimental model using the mode shapes of the finite element one.

Being y_r the experimental displacements (12 by the number of experimental samples), A the mode shapes extracted (12 by 2) and q the modal coordinates (2 by the number of experimental samples), the following relation can be formulated:

$$y_r = A_r \cdot q \tag{6.5}$$

$$\hat{q} = A_r{}^* \cdot y_r \tag{6.6}$$

Since $\hat{q}$ does not depend on the number of DOF, it is possible to apply again Equation 6.5, but in this case considering the same number of degrees of freedom as the finite element model.

$$y_e = A_e \cdot \hat{q} \tag{6.7}$$

In equation 6.7, y_e corresponds to the simulated displacements (264 by the number of simulated samples) and Ae corresponds to the mode shapes extracted from the finite element method (264 by 2). It is important to check them to ensure they correspond to the first two of the experimental model.

Knowing the node that corresponds with the centre of the plate, using y_e it is possible to check the displacements and make sure that the transformation matrix T from Equation 6.4 is correct.

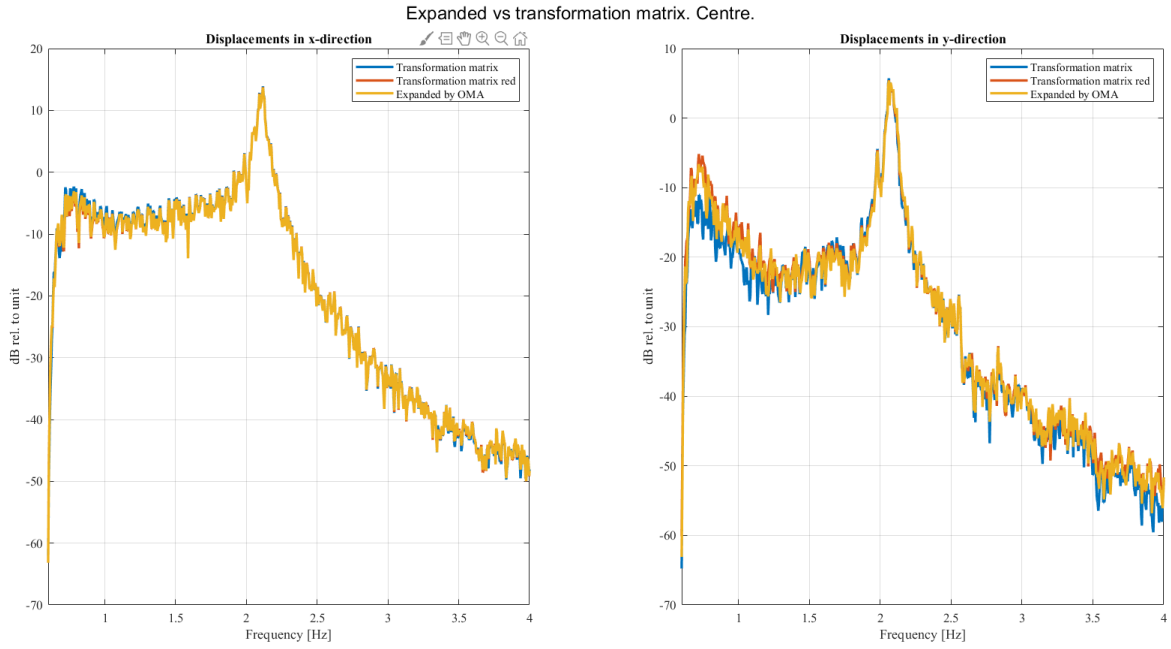

Figure 6.5. Spectral comparison of the displacements at the centre of the plate using the transformation matrix and the modal expansion. Test 71.

As it can be seen in Figure 6.5, the displacements from both methods are in accordance, so it can be assumed that the displacements calculated in the centre are accurate.

An alternate method of making sure that the transformation matrix works is to compare if the displacements in the centre deviate from the rest of the corners. As can be seen in Figure 6.6, the results show a good agreement.

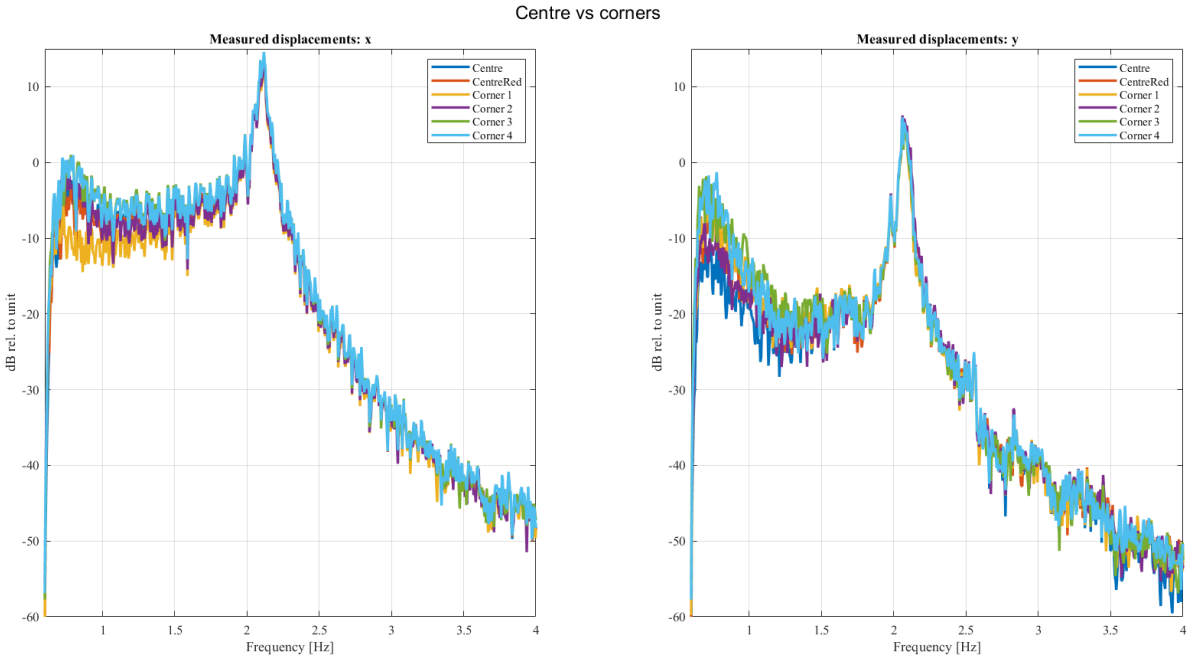

Figure 6.6. Spectral comparison of the displacements at each corner and centre. Test 71.

6.2. Comparison with Measured Displacements

Finally, the core of the project consisted of validating the wave simulation code. As stated previously, this was done comparing the displacements in the platform at the top of the monopile. More specifically, at the centre of the platform to reduce the influence of a possible torsion in the monopile. Of course, this means that the displacements in the vertical direction were neglected.

Before comparing the displacements at the centre, and since they were already obtained from the code, it was appropriate to also relate the displacements in the six chosen DOF.

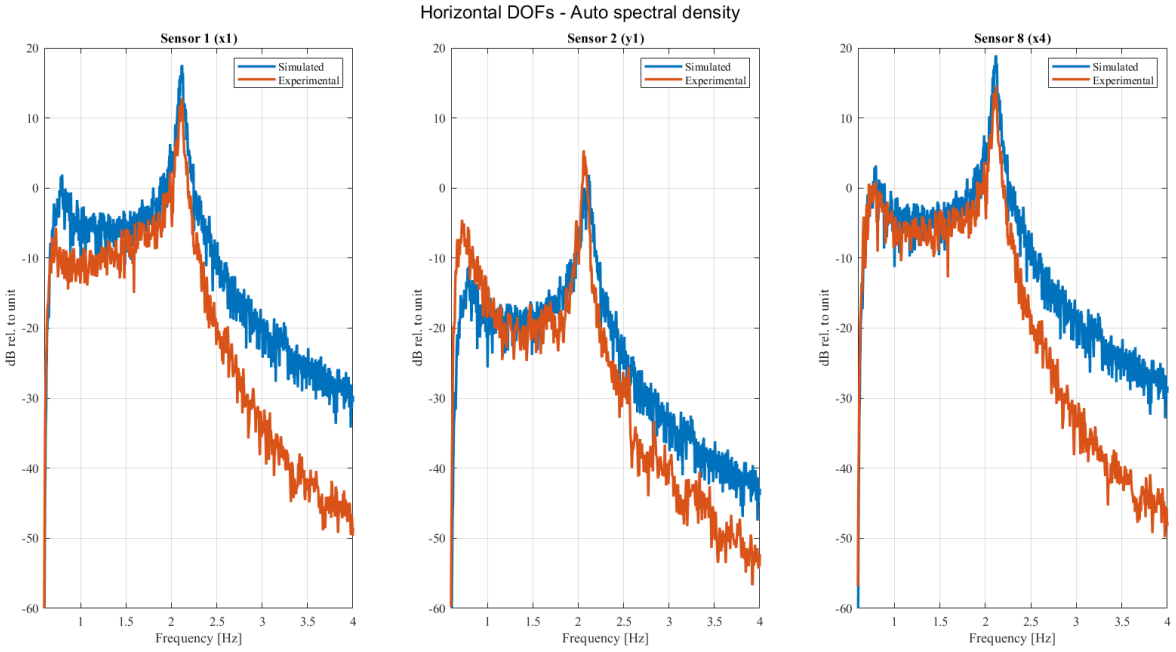

Figure 6.7. Spectral comparison of the displacements in the corners (x_1, y_1, x_4). Test 71.

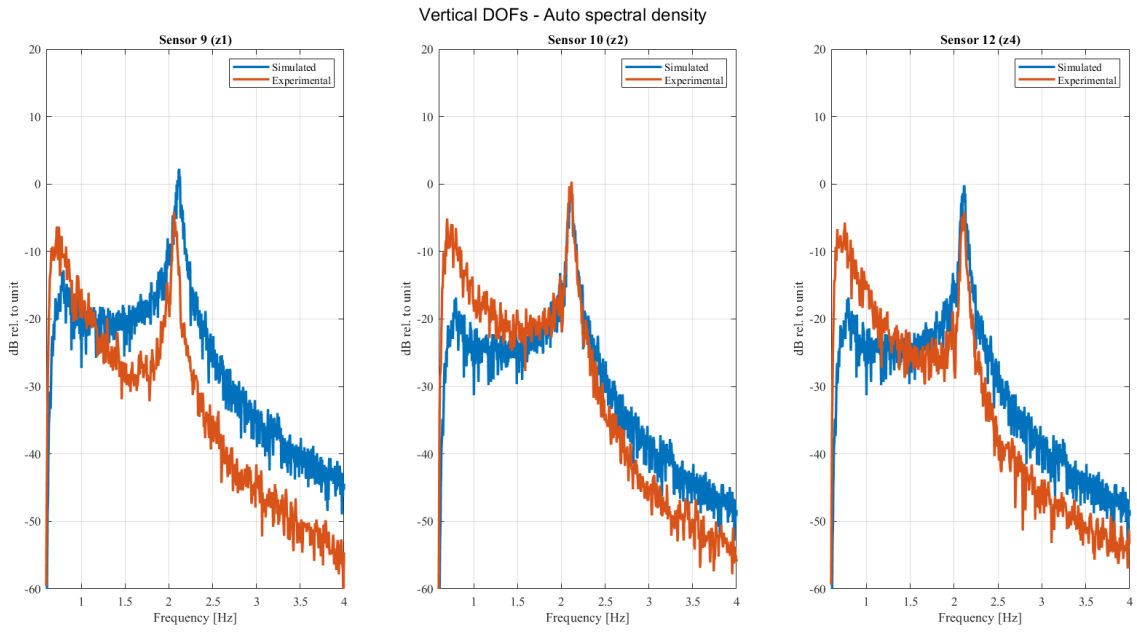

Figure 6.8. Spectral comparison of the displacements in the corners (z_1, z_2, z_4). Test 71.

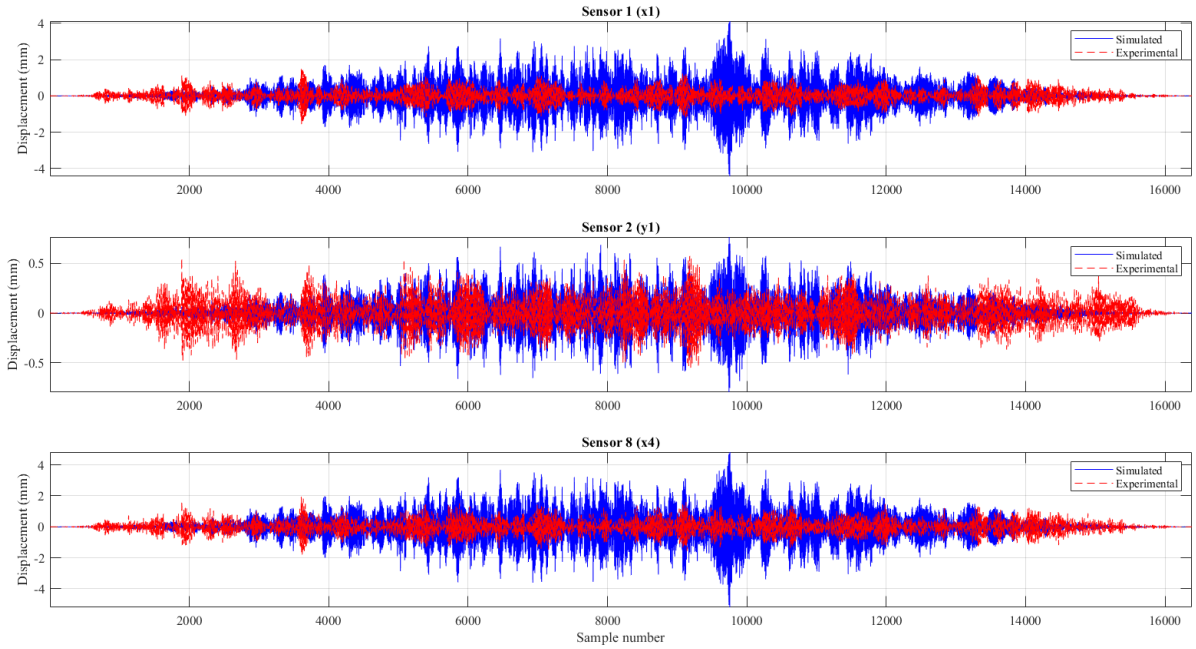

Figure 6.9. Time series comparison of the displacements in the corners (x_1, y_1, x_4). Test 71.

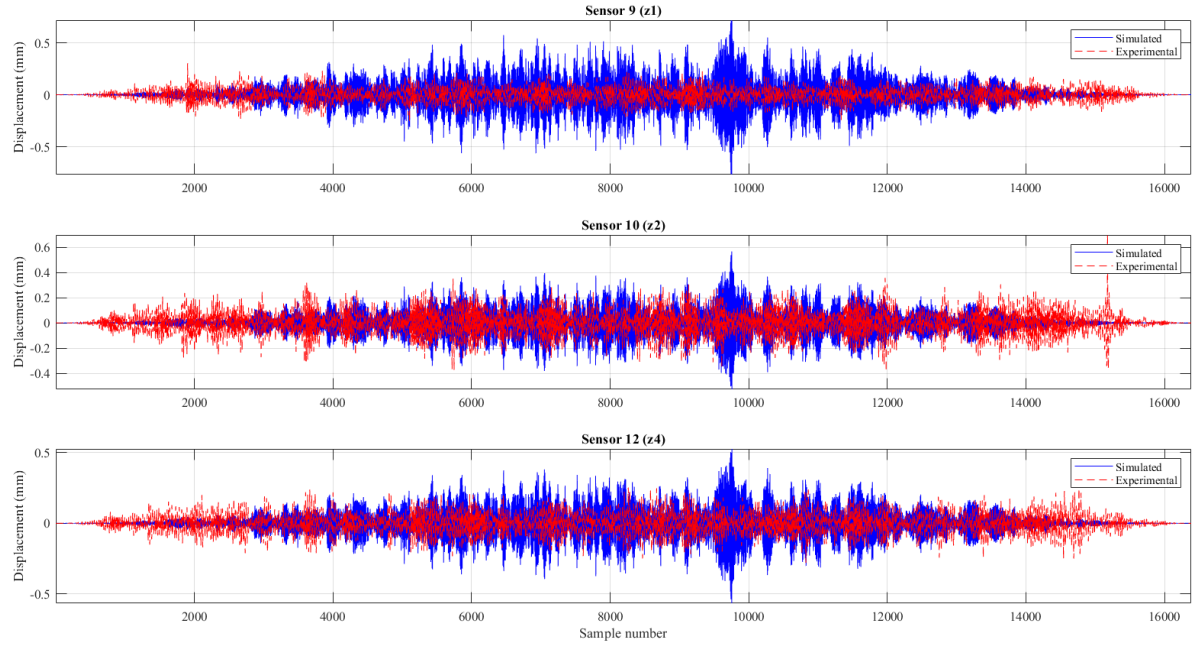

Figure 6.10. Time series comparison of the displacements in the corners (z_1, z_2, z_4). Test 71.

From Figure 6.7, one could say that the script simulates correctly the displacements in the x direction until the natural frequency is reached. After the natural frequency a clear divergence appears, with the simulated displacements having a much greater amplitude than the experimental. In the y direction, this divergence does not seem to be as important and the code makes a good job simulating the experimental movements. The z direction seems to indicate a more important problem with bigger experimental displacements at the beginning and lower after the peak: it seems that the energy bed of the experimental displacements is steeper than the simulated ones. This could be because no torsional mode was detected in the experimental model but in the finite element model, it was identified at around 12 Hz (Table 4.1), which could leave some residual energy in low frequencies. Looking at the displacements in the time domain (Figures 6.9 and 6.10), it seems clear that the simulated displacements in the x direction will be much higher than the experimental.

Observing the displacements in the centre (Figure 6.11) in the x direction again, everything seems correct until the natural frequency, where the experimental displacements experience a much steeper curve than the simulated ones. In the y direction this does not seem to be the case, but it fails to equal the magnitude of the displacements at low frequencies (<1 Hz). This is probably due to the static wave load.

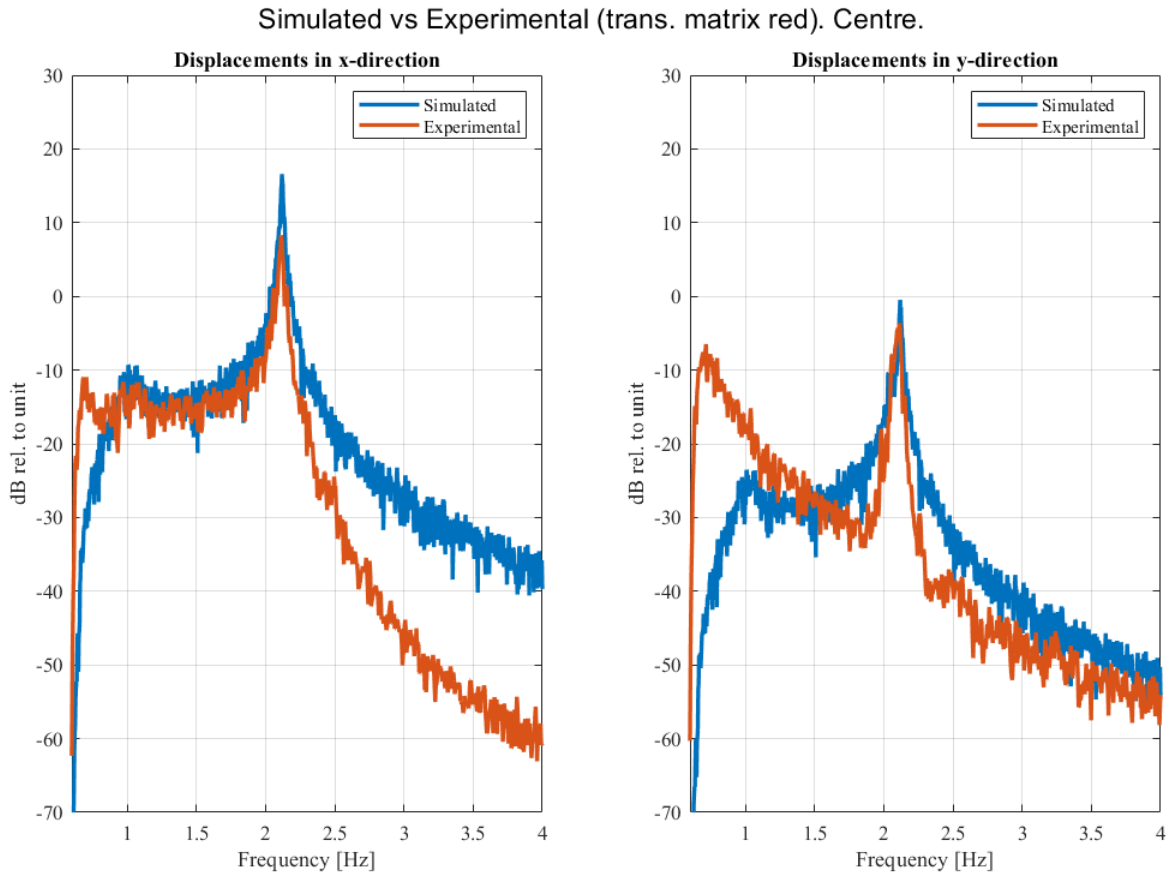

Figure 6.11. Spectral comparison of the displacements in the centre. Test 71.

Before any conclusions are drawn, it is relevant to note that these diagrams (Figures 6.7 to 6.11) only represent test number 70. To evaluate correctly the displacements in these directions it is important to review all the tests as seen in Tables 6.1 to 6.3.

			CENTRE X			CENTRE Y		
Test	H_s	T_p	SIM	EXP	FACT.	SIM	EXP	FACT.
70	0.023	1.00	0.4065	0.1669	2.44	0.0495	0.0649	0.76
73	0.038	1.00	0.6357	0.2853	2.23	0.0819	0.0961	0.85
69	0.066	1.22	0.7013	0.3419	2.05	0.0889	0.1172	0.76
67	0.076	1.26	0.6550	0.3197	2.05	0.0907	0.1057	0.86
72	0.078	1.17	0.8783	0.4027	2.18	0.1063	0.1336	0.80
75	0.080	1.14	0.8985	0.3718	2.42	0.1128	0.1298	0.87
65	0.085	1.29	0.7365	0.3679	2.00	0.1018	0.1280	0.80
71	0.094	1.29	0.8284	0.3689	2.25	0.1101	0.1413	0.78
66	0.124	1.65	0.7428	0.3685	2.02	0.0885	0.1868	0.47
MEAN					2.18			0.77

Table 6.1. Comparison between the standard deviation of the simulated displacements and the standard deviation of the experimental ones in the centre of the platform. H_s in metres and T_p in seconds. Fact. is the ratio between the simulated and the experimental displacements.

			SENSOR 1 (X_1)			SENSOR 2 (Y_1)			SENSOR 8 (X_4)		
Test	H_s	T_p	SIM	EXP	FACT.	SIM	EXP	FACT.	SIM	EXP	FACT.
70	0.023	1.00	0.372	0.152	2.45	0.070	0.057	1.23	0.441	0.188	2.35
73	0.038	1.00	0.585	0.258	2.27	0.110	0.089	1.24	0.686	0.317	2.16
69	0.066	1.22	0.646	0.308	2.10	0.122	0.110	1.11	0.757	0.381	1.99
67	0.076	1.26	0.603	0.286	2.11	0.121	0.104	1.16	0.707	0.361	1.96
72	0.078	1.17	0.806	0.362	2.23	0.143	0.125	1.14	0.879	0.448	1.96
75	0.080	1.14	0.829	0.334	2.48	0.155	0.127	1.22	0.968	0.415	2.33
65	0.085	1.29	0.679	0.318	2.14	0.136	0.125	1.09	0.794	0.400	1.99
71	0.094	1.29	0.764	0.330	2.32	0.148	0.137	1.08	0.893	0.415	2.15
66	0.124	1.65	0.685	0.334	2.05	0.124	0.181	0.69	0.801	0.410	1.95
MEAN					2.24			1.11			2.09

Table 6.2. Comparison between the standard deviation of the simulated displacements and the standard deviation of the experimental ones at the corners (x1, y1, x4). Hs in metres and Tp in seconds. Fact. is the ratio between the simulated and the experimental displacements.

			SENSOR 9 (Z_1)			SENSOR 10 (Z_2)			SENSOR 12 (Z_4)		
Test	H_s	T_p	SIM	EXP	FACT.	SIM	EXP	FACT.	SIM	EXP	FACT.
70	0.023	1.00	0.106	0.048	2.22	0.048	0.056	0.86	0.045	0.054	0.83
73	0.038	1.00	0.102	0.053	1.92	0.075	0.100	0.75	0.075	0.060	1.25
69	0.066	1.22	0.113	0.059	1.92	0.082	0.083	0.99	0.082	0.068	1.21
67	0.076	1.26	0.107	0.059	1.81	0.076	0.079	0.96	0.076	0.067	1.13
72	0.078	1.17	0.127	0.063	2.02	0.095	0.093	1.02	0.095	0.069	1.38
75	0.080	1.14	0.145	0.063	2.30	0.105	0.138	0.76	0.105	0.068	1.54
65	0.085	1.29	0.121	0.063	1.92	0.084	0.086	0.98	0.084	0.066	1.27
71	0.094	1.29	0.135	0.064	2.11	0.096	0.091	1.05	0.096	0.070	1.37
66	0.124	1.65	0.119	0.075	1.59	0.088	0.100	0.88	0.088	0.070	1.26
MEAN					1.98			0.92			1.25

Table 6.3. Comparison between the standard deviation of the simulated displacements and the standard deviation of the experimental ones at the corners (z_1, z_2, z_4). H_s in metres and T_p in seconds. Fact. is the ratio between the simulated and the experimental displacements.

The simulated displacements in the x direction require an amplifying coefficient of value 2.09-2.24 to be similar to the experimental ones, see Tables 6.1 and 6.2.

About the y direction, if one looked at the corner (Table 6.2) it would seem that it is almost correct, but checking the value at the centre (Table 6.1) seems to indicate that there is a rotation present, as the value in the centre is inferior to the one in the corner.

To a certain extent, it was expected that the simulated displacements would give higher values. This is because the simulations are based on the linear wave theory and in accordance with the Morison formulae, whilst considering conservative values of drag and inertia coefficients.

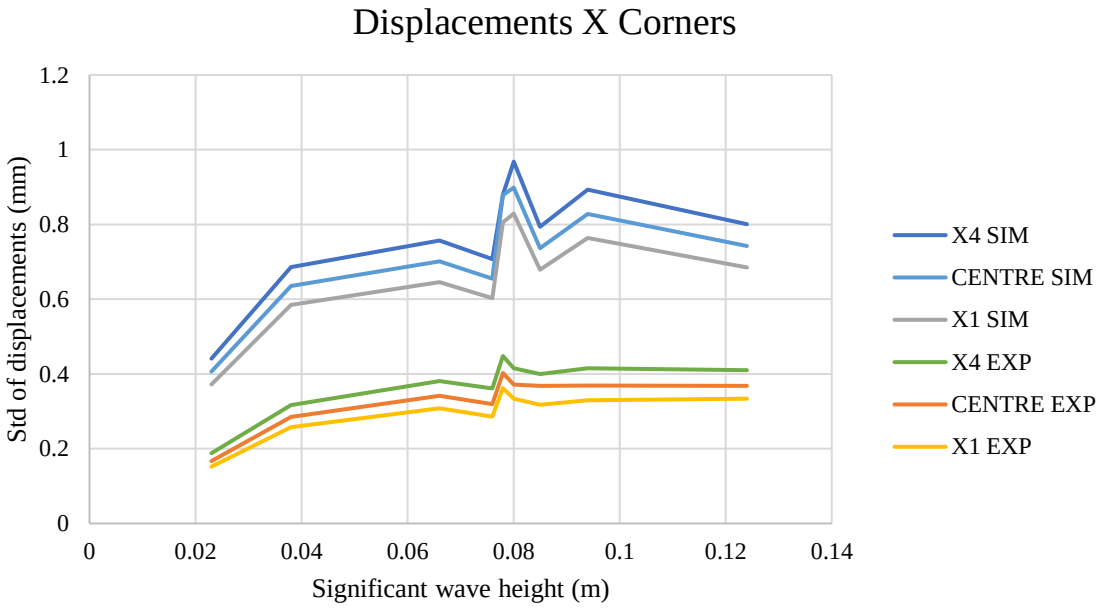

Figure 6.12. Relation between significant wave height and the standard deviation of the displacements in the *x* direction at different points of the platform.

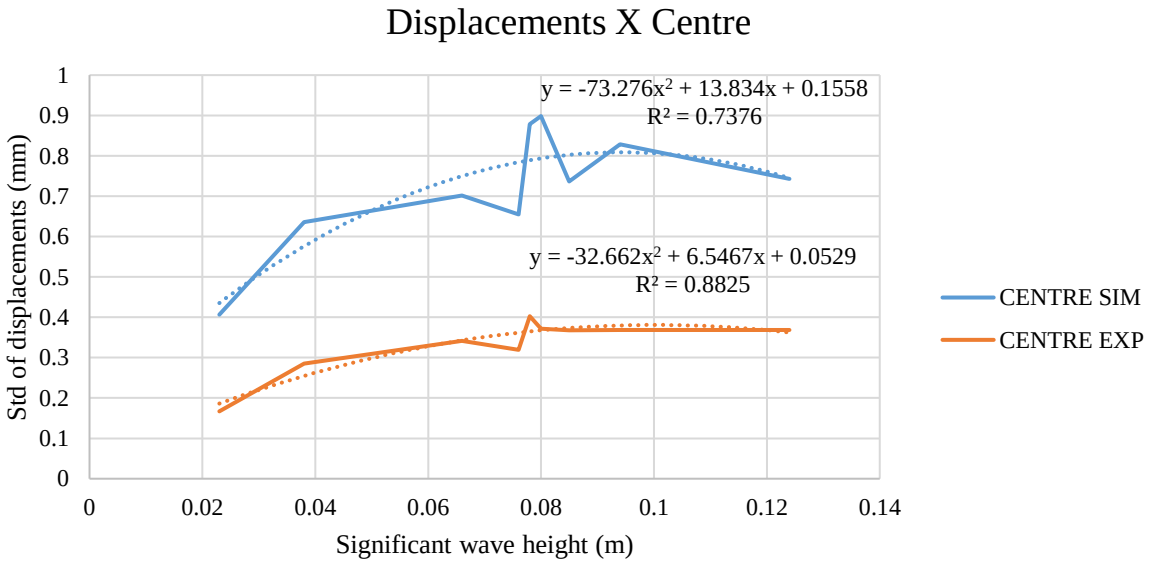

Figure 6.13. Relation between significant wave height and the standard deviation of the displacements in the *x* direction at the centre of the platform with a possible tendency line.

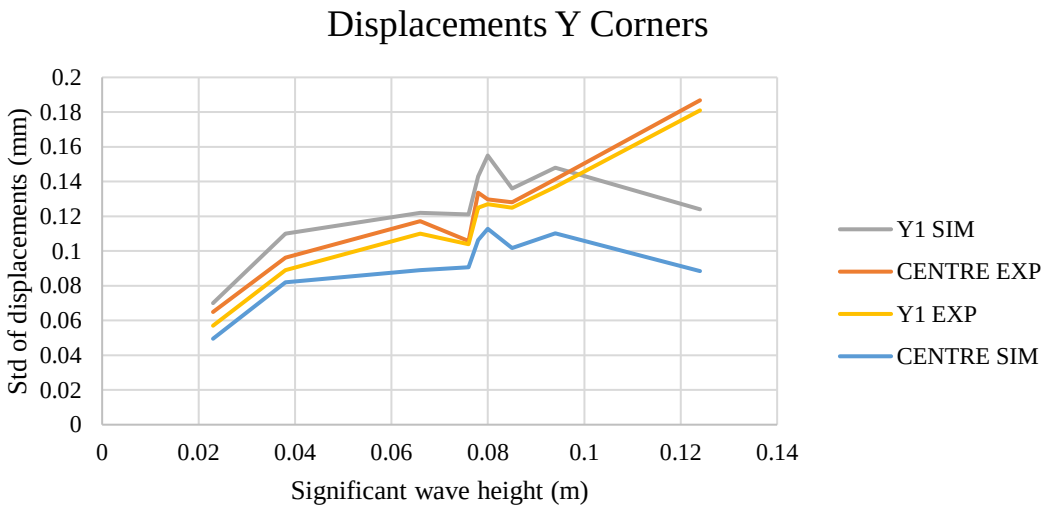

Figure 6.14. Relation between significant wave height and the standard deviation of the displacements in the *y* direction at different points of the platform.

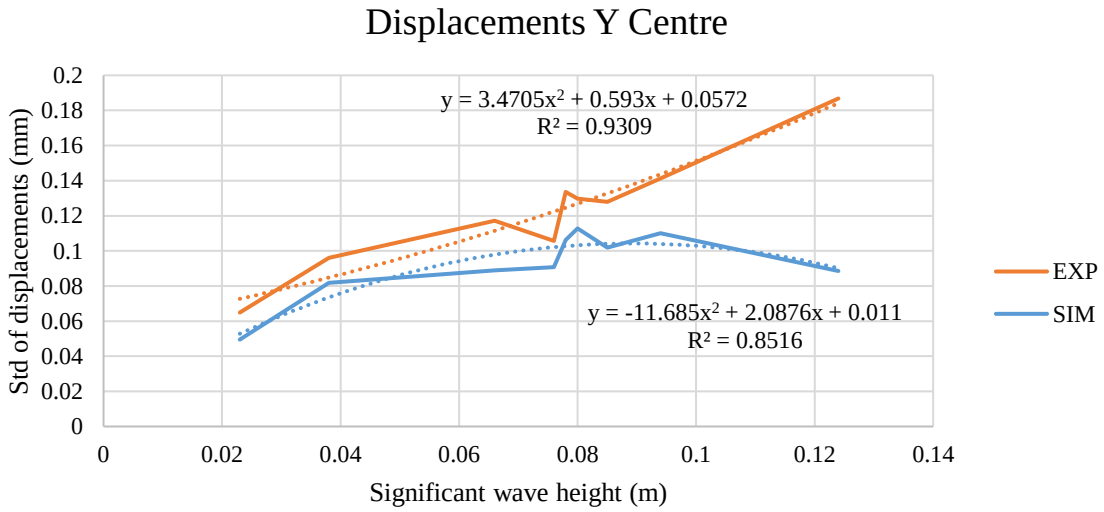

Figure 6.15. Relation between significant wave height and the standard deviation of the displacements in the *y* direction at the centre of the platform with a possible tendency line.

Displaying the standard deviation of the displacements against the significant wave height makes it possible to observe a slight correlation (Figures 6.13 and 6.15). However, there are not enough samples to obtain a reliable equation with a coefficient of determination higher than 0.95.

In Figure 6.12, it is clear that there are two different sets: the three simulated displacements and the three experimental. Although a similar trend is shown throughout these two individual sets, within each, there is a vertical offset between the curves.

In Figure 6.14, there are again two different sets of curves, the two simulated displacements and the two experimental. Each set follows a similar trend, until the point with the highest significant wave height where a clear divergence is shown.

Furthermore, after a continuous growth along the significant wave height, the peak period shows a decline around 0.08 m, which creates a disturbance in all the curves.

7. Conclusions and Further Study

As stated throughout this thesis, the objective was to validate a wave simulation code. This code is needed to generate a high amount of reliable data in order to simulate the force that waves could apply to an offshore structure. To achieve this, the displacements of a scaled model placed in a wave flume were compared with the displacements of a finite element model under the forces recreated by the wave simulation code. After comparing the displacements at the top of the model at multiple points and directions, various conclusions were drawn.

The wave simulation code functions to efficiently recreate the displacements in the x direction until the natural frequency of the model (<2 Hz) but for higher frequencies it was found to be less accurate, as the simulated displacements were superior to the experimental ones. From this, the overall standard deviation of the simulated displacements was found to be more than 2 times greater than that of the experimental displacements.

The wave simulation code works reliably by reproducing the displacements in the y direction only around the natural frequency of the model (2 Hz) but fails to be accurate for lower frequencies. For higher frequencies, it is more accurate than in the x direction. This leads to a standard deviation of the simulated code being similar to that of the experiments by a factor of 0.77 to 1.11 depending on the point of study, which relates to the notion of a possible rotation.

Apart from the validation of the displacements, in the results there was a slight relation between the significant wave height and the displacements, but the data provided was found to be insufficient.

It is important to mention that it was expected that the simulated displacements were to be higher than the experimental ones because they are based on the linear wave theory and Morison forces. This was done using conservative values for the drag and inertia coefficients.

Overall, this code should be tested thoroughly, as at present it is not entirely reliable. Further experiments should be performed, with a wider variety in the sea states and a greater number of tests carried out for each wave parameter. Another recommended practice would be the redundancy of the sampling, to ensure that there are no defectives sensors.

Finally, further work may be carried out to establish a relationship between the already measured strains of the scaled model and those that could be obtained from the finite element model. Although the study of the strains in the monopile was not addressed in this thesis, it is an additional parameter that could be monitored to validate the wave simulation code.

8. Bibliography

[1] Brincker, R., & Ventura, C. (2015). *Introduction to operational modal analysis*. John Wiley & Sons.

[2] Nabuco, Bruna (2018). Monopile Experiments in a Wave Flume for Operational Modal Analysis (OMA). Denmark Technical University (DTU)

[3] DNV, G. (2014). Environmental conditions and environmental loads (DNV-RP-C205). *Det Norske Veritas AS, Oslo*.

[4] Avitabile, P., & O'Callahan, J. C. (1995, February). Mass and stiffness orthogonality checks without a mass or stiffness matrix. In *PROCEEDINGS-SPIE THE INTERNATIONAL SOCIETY FOR OPTICAL ENGINEERING* (pp. 1516). SPIE INTERNATIONAL SOCIETY FOR OPTICAL.

[5] Amador, S., Juul, M., Friis, T., & Brincker, R. (2019). Finite element model updating using the local correspondence principle. In *Topics in Modal Analysis & Testing, Volume 9* (pp. 309-314). Springer, Cham.

[6] Pierson Jr, W. J., & Moskowitz, L. (1964). A proposed spectral form for fully developed wind seas based on the similarity theory of SA Kitaigorodskii. *Journal of geophysical research*, *69*(24), 5181-5190.

[7] Hasselmann, K., Barnett, T.P., Bouws, E., Carlson, H., Cartwright, D.E., Enke, K., Ewing, J.A., Gienapp, H., Hasselmann, D.E., Kruseman, P., Meerburgh, A., Mul-ler, P., Olbers, D.J., Richter, K., Sell, W., and Walden, H., 1973, "Measurement of wind-wave growth and swell decay during the Joint Nort Sea Wave Project (JONSWAP)", Deutschen Hydrogr. Zeitschrift, Reihe A(8) No.12

[8] International Towing Tank Conference (2002). The Specialist Committee on Waves. *Final Report and Recommendations to the 23rd ITTC.*

[9] Stewart, R. H. (2008). *Introduction to physical oceanography*. Robert H. Stewart.

[10] Andersen P. & Nielsen S. (2019, January) *OMA Based Monitoring of a Wind Loaded Structure*. pps 5-10.

9. Appendix A - Technical Drawings of the Experimental Model

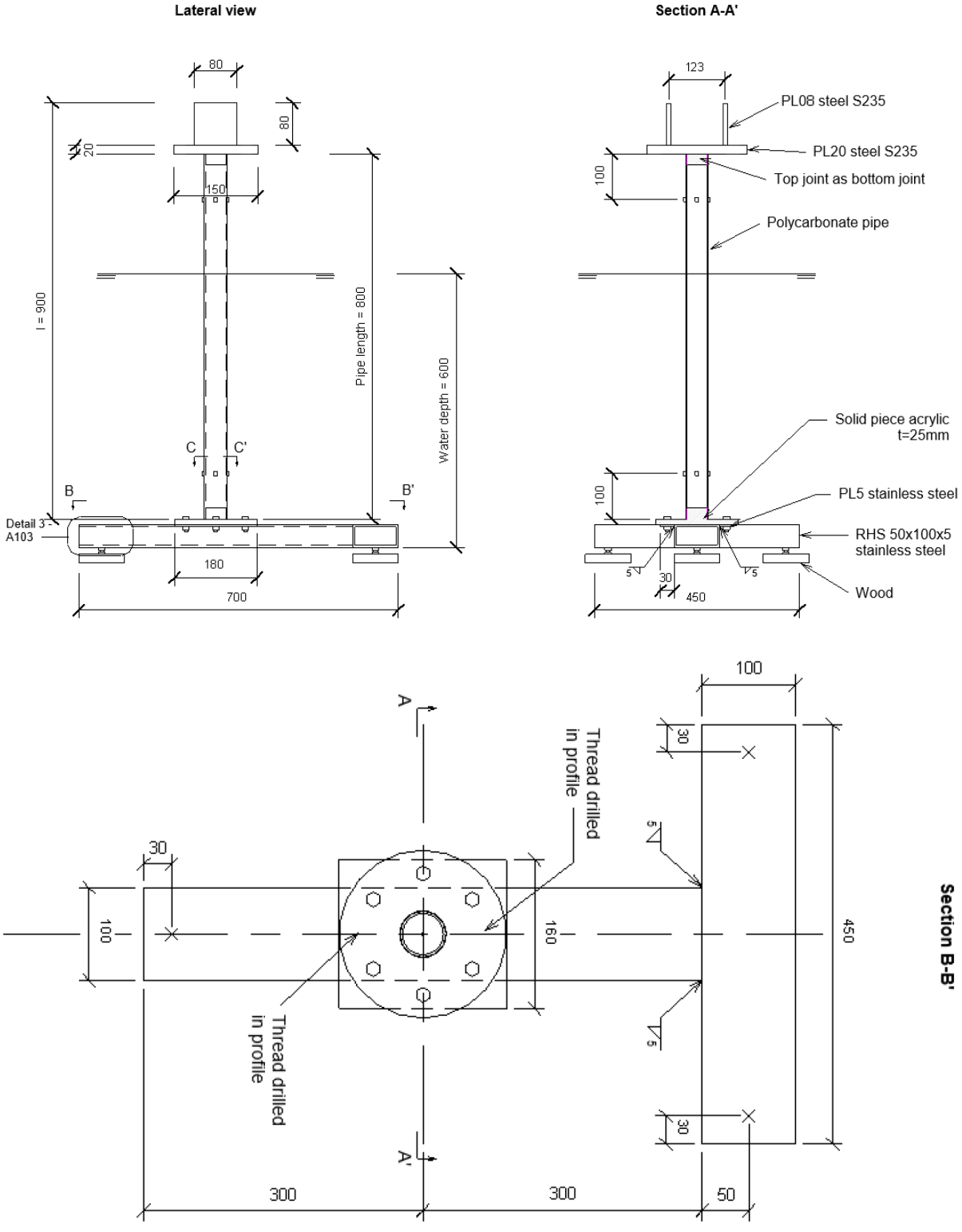

10. Appendix B – ANSYS Code for the FEM

The following code is the one used to create the finite element model used in this thesis. It is to be introduced in the software ANSYS 17.1.

```
/NOPR
!KEYW,PR_SET,1      $      KEYW,PR_STRUC,1      $      KEYW,PR_THERM,0      $
KEYW,PR_FLUID,0      $      KEYW,PR_ELMAG,0      $      KEYW,MAGNOD,0      $
KEYW,MAGEDG,0      $      KEYW,MAGHFE,0      $      KEYW,MAGELC,0      $
KEYW,PR_MULTI,0
!
/PREP7 ! preprocessor phase
! Element Type
ET,1,BEAM188
ET,2,SHELL181
!
! Material Properties
MP,EX,1,2.3E9 $ MP,PRXY,1,.3 $ MP,DENS,1,1200 !Polycarbonate
MP,EX,2,2.1E11 $ MP,PRXY,2,.305 $ MP,DENS,2,7850  !Steel
!
! Section
SECTYPE, 1, BEAM, CTUBE, CC1, $ SECDATA, 0.023, 0.025,
SECTYPE, 2, SHELL $ SECDATA,0.0207147654892877,2,0
SECTYPE, 3, SHELL $ SECDATA,0.008,2,0
!
! Define keypoints
K,1, 0.0000, 0.0000, 0.000
K,2, 0.0000, 0.0000, 0.810
!
K,3, -0.0750, 0.1100, 0.810
K,4, -0.0400, 0.1100, 0.810
K,5, 0.0000, 0.1100, 0.810
K,6, 0.0400, 0.1100, 0.810
K,7, 0.0750, 0.1100, 0.810
!
K,8, -0.0750, 0.0615, 0.810
K,9, -0.0400, 0.0615, 0.810
K,10, 0.0000, 0.0615, 0.810
K,11, 0.0400, 0.0615, 0.810
K,12, 0.0750, 0.0615, 0.810
!
K,13,-0.0750, 0.0000, 0.810
K,14,-0.0400, 0.0000, 0.810
K,15, 0.0400, 0.0000, 0.810
K,16, 0.0750, 0.0000, 0.810
!
K,17,-0.0750,-0.0615, 0.810
K,18,-0.0400,-0.0615, 0.810
K,19, 0.0000,-0.0615, 0.810
```

```
K,20, 0.0400,-0.0615, 0.810
K,21, 0.0750,-0.0615, 0.810
!
K,22,-0.0750,-0.1100, 0.810
K,23,-0.0400,-0.1100, 0.810
K,24, 0.0000,-0.1100, 0.810
K,25, 0.0400,-0.1100, 0.810
K,26, 0.0750,-0.1100, 0.810
!
K,27,-0.0400, 0.0615, 0.890
K,28, 0.0400, 0.0615, 0.890
K,29,-0.0400,-0.0615, 0.890
K,30, 0.0400,-0.0615, 0.890
!
! Define lines
L,1,2
!
! Associate lines with ET, MAT and SEC
LSEL, S, LINE,, 1, 1, 1, 0 $ LESIZE, ALL,,, 16, 1, 1 $ LATT, 1,, 1,,,, 1
!
! Generate mesh on all lines
ALLSEL, ALL, LINE $ LMESH, ALL
!
! Define areas
!
A, 3, 4, 9, 8
A, 4, 5,10, 9
A, 5, 6,11,10
A, 6, 7,12,11
!
A, 8, 9,14,13
A, 9,10, 2,14
A,10,11,15, 2
A,11,12,16,15
!
A,13,14,18,17
A,14, 2,19,18
A, 2,15,20,19
A,15,16,21,20
!
A,17,18,23,22
A,18,19,24,23
A,19,20,25,24
A,20,21,26,25
A, 9,11,28,27
A,18,20,30,29
!
LOCAL, 11, 0, 0, 0, 0
ASEL, S, AREA,, ALL, , , 0 $ AESIZE, ALL, 2.0,   ! AATT, MAT, REAL, TYPE, ESYS,
SECN
```

```
ASEL, S, AREA,,1,16 $ AATT, 2,, 2, 11, 2
ASEL, S, AREA,,17,18 $ AATT, 2,, 2, 11, 3
ALLSEL, ALL, AREA $ AMESH, ALL
!
! Finish Preprocessor and Export file
FINISH
ALLSEL, ALL, ALL
CDOPT,IGES
CDWRITE,ALL,'Monopile','cdb',,'Monopile','iges'
!
! Modal Analysis
/SOLU ! Enter solution mode
NSEL, S, LOC, Z, 0 $ D,ALL,,0,,,,UX,UY,UZ, ROTX, ROTY, ROTZ ! Boundary Conditions
ALLSEL, ALL, ALL
ANTYPE,2
MODOPT,LANB,10
EQSLV,SPAR
MXPAND,10, , ,1
LUMPM,0
PSTRES,0
WRFULL,YES
EMATWRITE,YES
SOLVE
FINISH
/AUX2
FILE,'file','full'
FINISH
*SMAT,MatK,D,IMPORT,FULL,file.full,STIFF
*SMAT,MatM,D,IMPORT,FULL,file.full,MASS
*VEC,VectMapB,I,IMPORT,FULL,file.full,BACK
*EXPORT,MatK,MMF,StiffMatMMF.mmf
*EXPORT,MatM,MMF,MassMatMMF.mmf
*EXPORT,VectMapB,MMF,MappingBMatMMF.mmf
FINISH
```

11. Appendix C – Generic Transformation Matrix

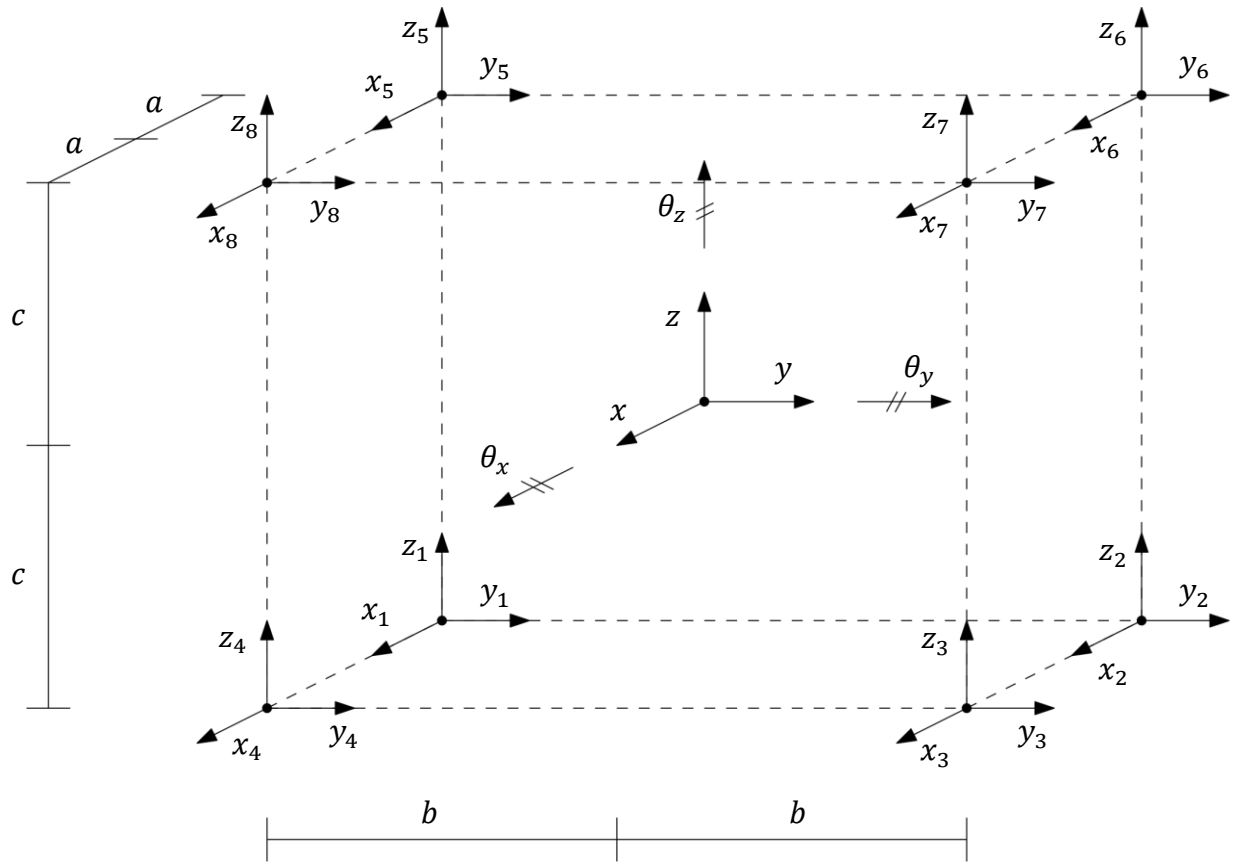

Figure C.1. Schematic proposing the distribution of eight sensors.

$$y = T \cdot \theta \tag{C.1}$$

Where y are the displacements in the corners and θ the displacements in the centre.

$$\theta' = \{x \;\; y \;\; z \;\; \theta_x \;\; \theta_y \;\; \theta_z\} \tag{C.2}$$

$$A = \begin{pmatrix} cos\theta & -sin\theta \\ sin\theta & cos\theta \end{pmatrix} \approx \begin{pmatrix} 1 & -\theta \\ \theta & 1 \end{pmatrix} \tag{C.3}$$

$$f_i = \widehat{v_i} - v_i = Av_i - v_i \tag{C.4}$$

11.1. Rotation around x axis

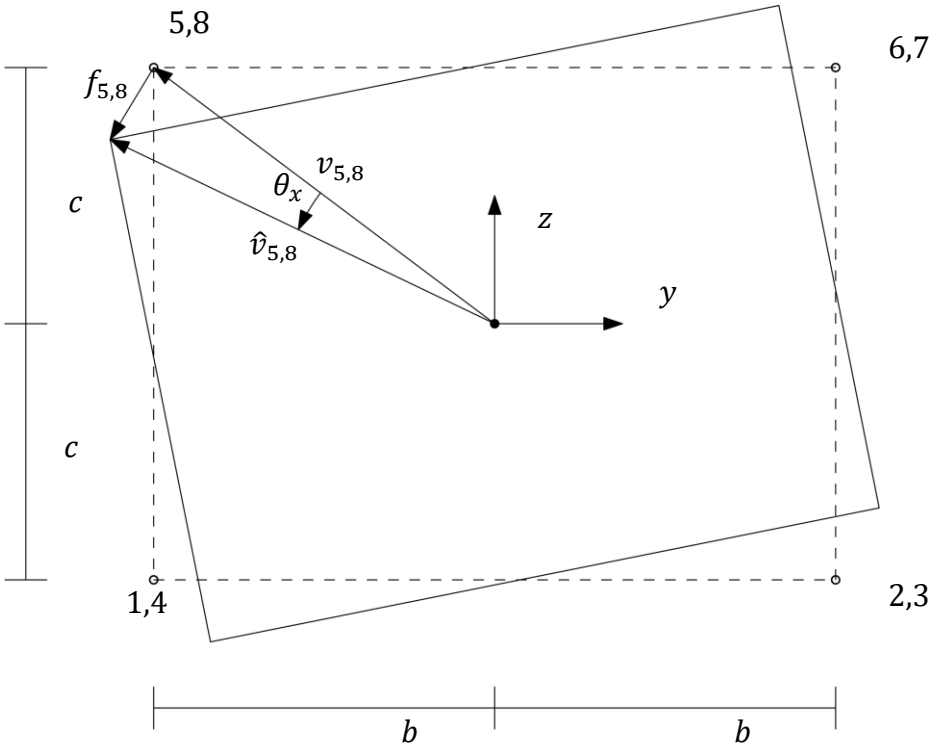

Figure C.2. Schematic depicting the rotation around x.

$$v_{1,4} = \begin{pmatrix} -b \\ -c \end{pmatrix}, v_{2,3} = \begin{pmatrix} b \\ -c \end{pmatrix}, v_{5,8} = \begin{pmatrix} -b \\ c \end{pmatrix}, v_{6,7} = \begin{pmatrix} b \\ c \end{pmatrix}$$

$$f_{1,4} = \begin{pmatrix} y_{1,4} \\ z_{1,4} \end{pmatrix} = \begin{pmatrix} c \\ -b \end{pmatrix} \theta_x, f_{2,3} = \begin{pmatrix} y_{2,3} \\ z_{2,3} \end{pmatrix} = \begin{pmatrix} c \\ b \end{pmatrix} \theta_x$$

$$f_{5,8} = \begin{pmatrix} y_{5,8} \\ z_{5,8} \end{pmatrix} = \begin{pmatrix} -c \\ -b \end{pmatrix} \theta_x, f_{6,7} = \begin{pmatrix} y_{6,7} \\ z_{6,7} \end{pmatrix} = \begin{pmatrix} -c \\ b \end{pmatrix} \theta_x$$

11.2. Rotation around y axis

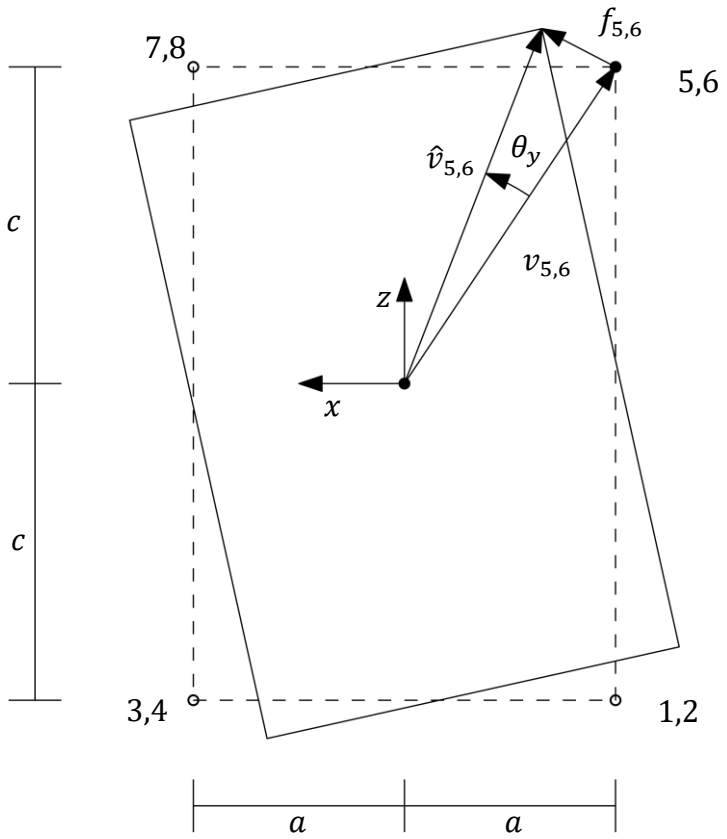

Figure C.3. Schematic depicting the rotation around y.

$$v_{1,2} = \begin{pmatrix} -c \\ -a \end{pmatrix}, v_{3,4} = \begin{pmatrix} -c \\ a \end{pmatrix}, v_{5,6} = \begin{pmatrix} c \\ -a \end{pmatrix}, v_{7,8} = \begin{pmatrix} c \\ a \end{pmatrix}$$

$$f_{1,2} = \begin{pmatrix} z_{1,2} \\ x_{1,2} \end{pmatrix} = \begin{pmatrix} a \\ -c \end{pmatrix} \theta_y, f_{3,4} = \begin{pmatrix} z_{3,4} \\ x_{3,4} \end{pmatrix} = \begin{pmatrix} -a \\ -c \end{pmatrix} \theta_y$$

$$f_{5,6} = \begin{pmatrix} z_{5,6} \\ x_{5,6} \end{pmatrix} = \begin{pmatrix} a \\ c \end{pmatrix} \theta_y, f_{7,8} = \begin{pmatrix} z_{7,8} \\ x_{7,8} \end{pmatrix} = \begin{pmatrix} -a \\ c \end{pmatrix} \theta_y$$

11.3. Rotation around z axis

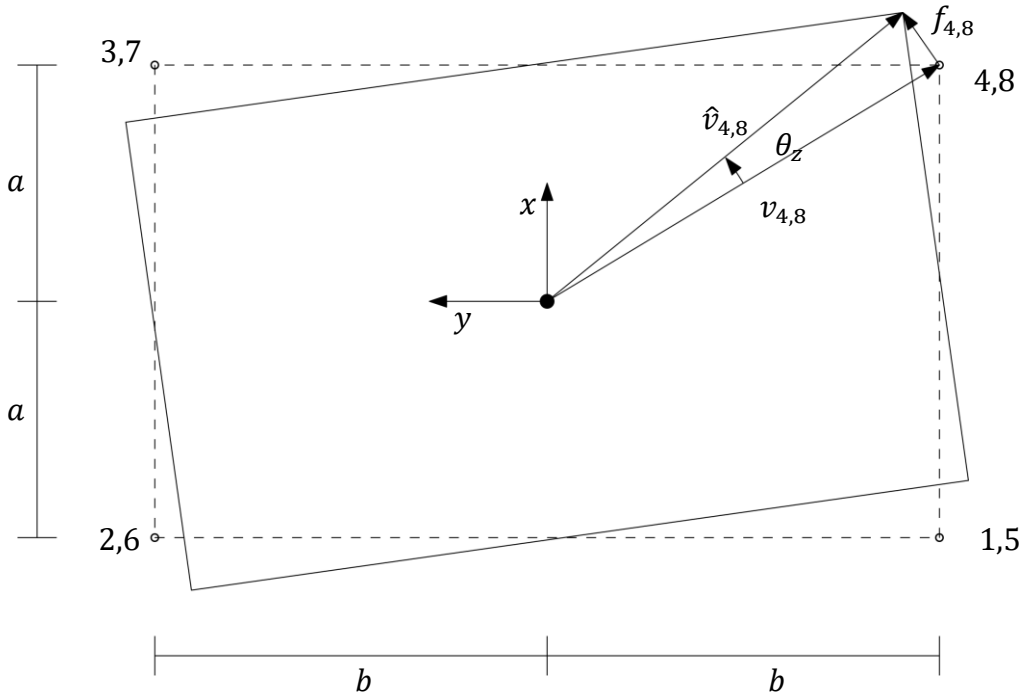

Figure C.4. Schematic depicting the rotation around z.

$$v_{1,5} = \begin{pmatrix} -a \\ -b \end{pmatrix}, v_{2,6} = \begin{pmatrix} -a \\ b \end{pmatrix}, v_{3,7} = \begin{pmatrix} a \\ b \end{pmatrix}, v_{4,8} = \begin{pmatrix} a \\ -b \end{pmatrix}$$

$$f_{1,5} = \begin{pmatrix} x_{1,5} \\ y_{1,5} \end{pmatrix} = \begin{pmatrix} b \\ -a \end{pmatrix} \theta_z, f_{2,6} = \begin{pmatrix} x_{2,6} \\ y_{2,6} \end{pmatrix} = \begin{pmatrix} -b \\ -a \end{pmatrix} \theta_z$$

$$f_{3,7} = \begin{pmatrix} x_{3,7} \\ y_{3,7} \end{pmatrix} = \begin{pmatrix} -b \\ a \end{pmatrix} \theta_z, f_{4,8} = \begin{pmatrix} x_{4,8} \\ y_{4,8} \end{pmatrix} = \begin{pmatrix} b \\ a \end{pmatrix} \theta_z$$

$$T = \left(\begin{array}{cccccc|c} 1 & 0 & 0 & 0 & -c & b & x_1 \\ 0 & 1 & 0 & c & 0 & -a & y_1 \\ 0 & 0 & 1 & -b & a & 0 & z_1 \\ 1 & 0 & 0 & 0 & -c & -b & x_2 \\ 0 & 1 & 0 & c & 0 & -a & y_2 \\ 0 & 0 & 1 & b & a & 0 & z_2 \\ 1 & 0 & 0 & 0 & -c & -b & x_3 \\ 0 & 1 & 0 & c & 0 & a & y_3 \\ 0 & 0 & 1 & b & -a & 0 & z_3 \\ 1 & 0 & 0 & 0 & -c & b & x_4 \\ 0 & 1 & 0 & c & 0 & a & y_4 \\ 0 & 0 & 1 & -b & -a & 0 & z_4 \\ 1 & 0 & 0 & 0 & c & b & x_5 \\ 0 & 1 & 0 & -c & 0 & -a & y_5 \\ 0 & 0 & 1 & -b & a & 0 & z_5 \\ 1 & 0 & 0 & 0 & c & -b & x_6 \\ 0 & 1 & 0 & -c & 0 & -a & y_6 \\ 0 & 0 & 1 & b & a & 0 & z_6 \\ 1 & 0 & 0 & 0 & c & -b & x_7 \\ 0 & 1 & 0 & -c & 0 & a & y_7 \\ 0 & 0 & 1 & b & -a & 0 & z_7 \\ 1 & 0 & 0 & 0 & c & b & x_8 \\ 0 & 1 & 0 & -c & 0 & a & y_8 \\ 0 & 0 & 1 & -b & -a & 0 & z_8 \end{array}\right) \qquad \text{(C.5)}$$